Open access • Posted Content • DOI:10.1101/808808

A functional corona around extracellular vesicles enhances angiogenesis during skin regeneration and signals in immune cells — Source link ☒

Martin Wolf, Rodolphe Poupardin, Patricia Ebner-Peking, André Cronemberger Andrade ...+17 more authors

Institutions: Paracelsus Private Medical University of Salzburg, Medical University of Vienna, Charité

Related papers:

- Supported Membrane Platform to Assess Surface Interactions between Extracellular Vesicles and Stromal Cells.

- Interaction of extracellular vesicles with endothelial cells under physiological flow conditions

- Cell-Matrix Interactions Regulate Functional Extracellular Vesicle Secretion from Mesenchymal Stromal Cells.

- Dendritic Cell-derived Extracellular Vesicles mediate Mesenchymal Stem/Stromal Cell recruitment.

- Characteristics and roles of extracellular vesicles released by epidermal keratinocytes.

Extracellular vesicles from therapeutic grade allogeneic human placental stromal cells induce angiogenesis and modulate immunity

Martin Wolf[1], Balazs Vari[1], Constantin Blöchl[2], Anna M Raninger[1], Rodolphe Poupardin[1], Cristien M Beez[3], Anna Hoog[1], Gabi Brachtl[1], Essi Eminger[1]; Heide-Marie Binder[1], Michaela Oeller[4], Andreas Spittler[5], Thomas Heuser[6], Astrid Obermayer[2], Martina Seifert[3], Christian G Huber[2], Katharina Schallmoser[4], Hans-Dieter Volk[3], Dirk Strunk[1]

[1]Cell Therapy Institute, Spinal Cord Injury and Tissue Regeneration Center Salzburg (SCI-TReCS), Paracelsus Medical University (PMU), Salzburg, Austria

[2]Dept. of Biosciences, Paris Lodron University Salzburg

[3]*BCRT & Institute of Medical Immunology, Charite - Univeritätsmedizin Berlin, Germany*

[4]Department of Transfusion Medicine and SCI-TReCS, PMU, Salzburg, Austria

[5]Anna Spiegel Center of Translational Research, Medical University, Vienna

[6]Vienna Biocenter Core Facilities, Medical University, Vienna

Authorship Contributions:

Conception and design: M Wolf and D Strunk.

Development of methodology: M Wolf, B Vari, AM Raninger, A Spittler, D Strunk

Acquisition of data: M Wolf, B Vari, C Blöchl, AM Raninger, CM Beez, A Hoog, E Eminger, G Brachtl, T Heuser, M Oeller, A Spittler

Analysis and interpretation of data: M Wolf, B Vari, C Blöchl, R Poupardin, HM Binder, M Seifert, G Brachtl, D Strunk

Writing of the manuscript: M Wolf and D Strunk

Review and/or revision of the manuscript: K Schallmoser, M Seifert, CG Huber, H-D Volk

Administrative, technical, or material support: R Ofir

Study supervision: Dirk Strunk

October 17, 2019

ABSTRACT *(221 words)*

Allogeneic regenerative cell therapy has shown surprising results despite lack of engraftment of the transplanted cells. Their efficacy was so far considered to be mostly due to secreted trophic factors. We hypothesized that extracellular vesicles (EVs) can also contribute to their mode of action. Here we provide evidence that EVs derived from therapeutic placental-expanded (PLX) stromal cells are potent inducers of angiogenesis and modulate immune cell proliferation in a dose-dependent manner.

Crude EVs were enriched >100-fold from large volume PLX conditioned media via tangential flow filtration (TFF) as determined by tunable resistive pulse sensing (TRPS). Additional TFF purification was devised to separate EVs from cell-secreted soluble factors. EV identity was confirmed by western blot, calcein-based flow cytometry and electron microscopy. Surface marker profiling of tetraspanin-positive EVs identified expression of cell- and matrix-interacting adhesion molecules. Differential tandem mass tag proteomics comparing PLX-EVs to PLX-derived soluble factors revealed significant differential enrichment of 258 proteins in purified PLX-EVs involved in angiogenesis, cell movement and immune system signaling. At the functional level, PLX-EVs and cells inhibited T cell mitogenesis. PLX-EVs and soluble factors displayed dose-dependent proangiogenic potential by enhancing tube-like structure formation *in vitro*.

Our findings indicate that the mode of PLX action involves an EV-mediated proangiogenic function and immune response modulation that may help explaining clinical efficacy beyond presence of the transplanted allogeneic cells.

KEYWORDS: Placental-expanded stromal cells (PLX), extracellular vesicles (EV), Therapy, Immunomodulation, Angiogenesis, regenerative medicine

October 17, 2019

INTRODUCTION

Peripheral artery disease (PAD) affects >10% of the European elderly population. Critical limb ischemia (CLI) is an end stage of PAD resulting in high amputation rates and is associated with increased risk for cardiovascular events and death. Allogeneic placental-expanded (PLX) stromal cells are currently evaluated in a clinical phase III trial (NCT03006770) challenging their efficiency as an advanced CLI therapy [1]. The regenerative potential of these placental cells is not restricted to CLI as evidenced by their hematopoietic support activity [2], a capacity to protect from radiation injury [3], and their current investigation for improving muscle injury regeneration in patients after hip arthroplasty [4]. Their mode of action has mainly been considered to be due to secretion of a variety of cytokines and growth factors that can promote angiogenesis, cell recruitment, migration, proliferation, and differentiation [5]. The general immunomodulatory capacity of stromal cells has also been hypothesized to exert beneficial effects on the local and/or systemic immune response [5], [6].

Extracellular vesicles (EVs) are a heterogeneous family of generally nano-sized membrane-coated vesicular structures derived from most if not all cell types [7]. EVs comprise prototypic endosomal-derived exosomes which are assembled and released via multivesicular bodies as well as directly cell membrane-derived sub-micron sized so-called microvesicles and apoptotic bodies [8], [9]. Conceptually, EVs transport their protein, lipid and nucleic acid cargo to target sites allowing for action also over distance [9], [10]. Address code molecules displayed on the EV surface may contribute to target specificity [11].

Inspired by the multiplicity of functions EVs can comply within intercellular communication paving their way towards clinical applicability [8], [12], we hypothesized that PLX cells, representing a widely applicable allogeneic cell therapy, can secrete EVs that bear the capacity to contribute to their mode of action. We used conditioned media obtained after short-term propagation of clinical grade PLX cell products under animal serum-free conditions to separate EVs from their corresponding PLX-derived soluble factors for comparative proteomic analysis and to test their influence on endothelial cell (EC) and immune cell functions (**Fig.S1**). Results obtained as part of a European funded research project (http://www.pace-h2020.eu/) indicated proangiogenic and immunomodulatory potency of PLX-derived EVs.

October 17, 2019
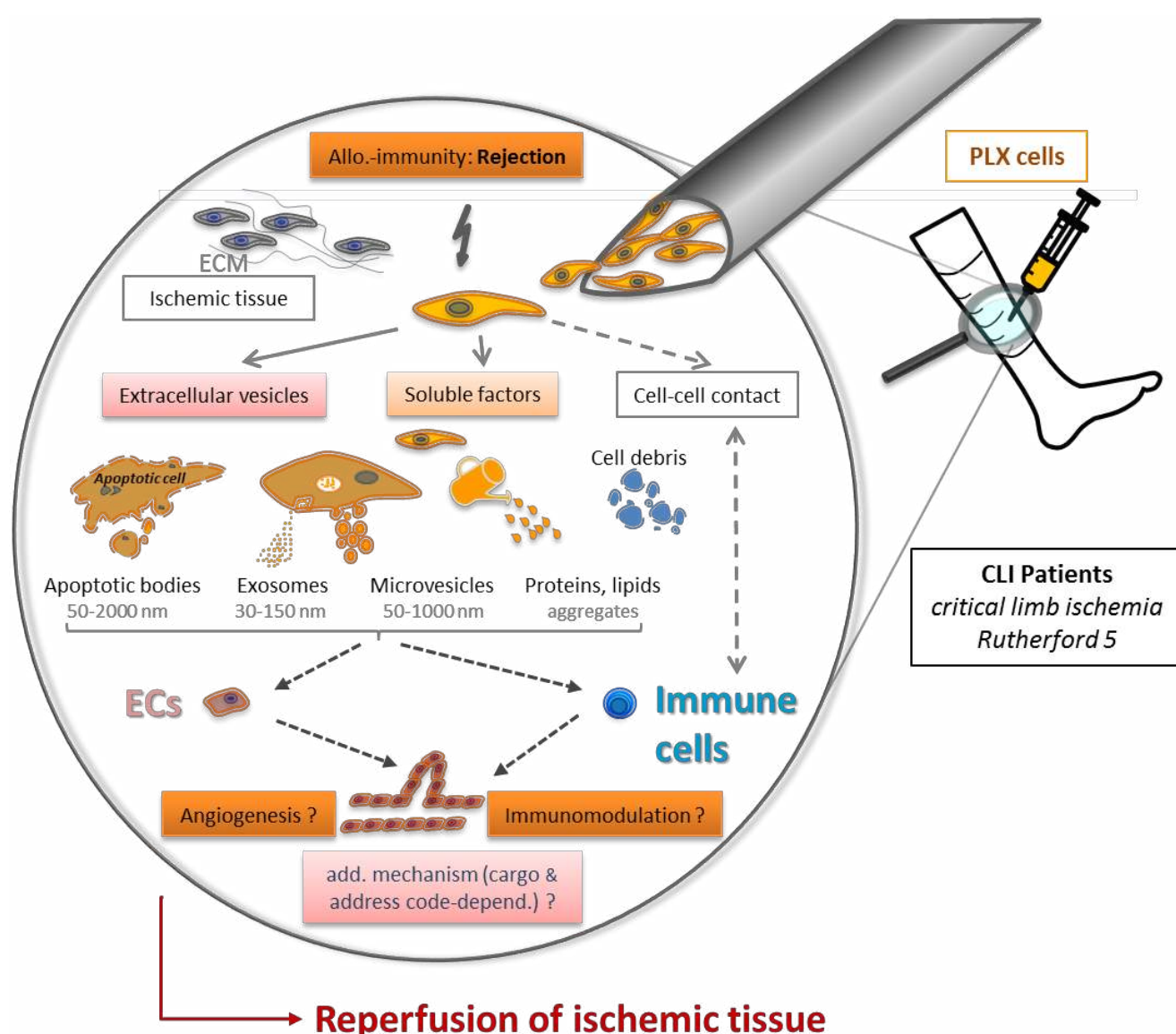
Figure S1. Hypothetic mode of action of allogeneic PLX stromal cells. Allogeneic placental-expanded (PLX) cells are considered to be rejected by the host immune system after local injection. The mode of action may include a temporary direct (cell-cell contact) or indirect stimulation of endogenous (endothelial or perivascular or interstitial) progenitor cells as well as immune response modulation by various types of secreted factors eventually resulting in reperfusion of the ischemic tissue and ideally wound healing. In this study we focused on extracellular vesicles (EVs) compared to secreted soluble factors as potential mediators of PLX's biologic activity.

RESULTS

Physically defined media enable efficient cell-derived EV characterization

October 17, 2019

In initial experiments, we compared the particle count of standard media used at our institution for stromal cell culture to select a suitable medium for PLX cell-derived EV isolation. Alpha-modified minimum essential medium (α-MEM) as well as other conventional media supplemented with either fetal bovine serum (FBS) or pooled human platelet lysate (HPL) as published [13] contained mean $4 \times 10^8 - 3 \times 10^9$ particles/mL. Fibrinogen-depleted α-MEM (α-MEM*) which can be used without heparin, that otherwise might inhibit EV functions [14], [15], showed even higher particle counts up to 10^{10}/mL. Both ultracentrifugation (UCF) and tangential flow filtration (TFF) allowed for a significant depletion of serum- or plasma-derived EVs. We chose TFF in further experiments for better scalability and time saving purposes because efficient depletion of serum-EVs by UCF required up to 24 h centrifugation at 100,000 x g [16], [17]. Some but not all tested chemically defined serum-free media contained less than 10^8 particles/mL (**Fig.S2A**). Culturing PLX cells in regular fibrinogen-containing α-MEM/HPL resulted in a significant rise of EVs on top of the pre-existing HPL-derived EVs within six days. PLX cell culture in TFF particle-depleted α-MEM*/TFF or in defined media resulted in a significantly elevated particle count after six day culture thus indicating effective release of PLX-EVs under these conditions (**Fig.S2B**). Time course analysis confirmed significant production of PLX-EVs under both α-MEM*/TFF and chemically defined serum-free medium conditions for up to six days (i.e., 3 x 48 h conditioned medium [CM] harvest periods; **Fig.S2C**). Tunable resistive pulse sensing (TRPS) size distribution showed a more heterogeneous particle composition under serum-free defined conditions including measurably larger particles (**Fig.S2D**). For reasons of efficiency, we chose fibrinogen-depleted and particle-depleted α-MEM*/TFF for further experiments.

We next devised a standardized high content process for EV production (**Fig.1**) based on previous results [18]. Large volumes of fibrinogen-depleted α-MEM* (n x 500 mL) were first depleted for platelet-rich plasma- and serum-derived particles (including EVs) before use in large-scale PLX culture (**Fig.1A**). Following protocols previously established for large scale fully functional bone marrow stromal cell propagation [19]–[22], CM was harvested from cell factories after 48 h periods in particle depleted α-MEM*/TFF (**Fig.1B**) and subjected to 100x concentration of crude PLX-EVs (**Fig.1C**). These crude EV preparations, containing PLX-EVs admixed with concentrated proteins, were separated from the soluble factor fraction that was obtained as the TFF permeate. Further purification of the crude EV preparations with another TFF cycle allowed producing purified EVs.

5

October 17, 2019
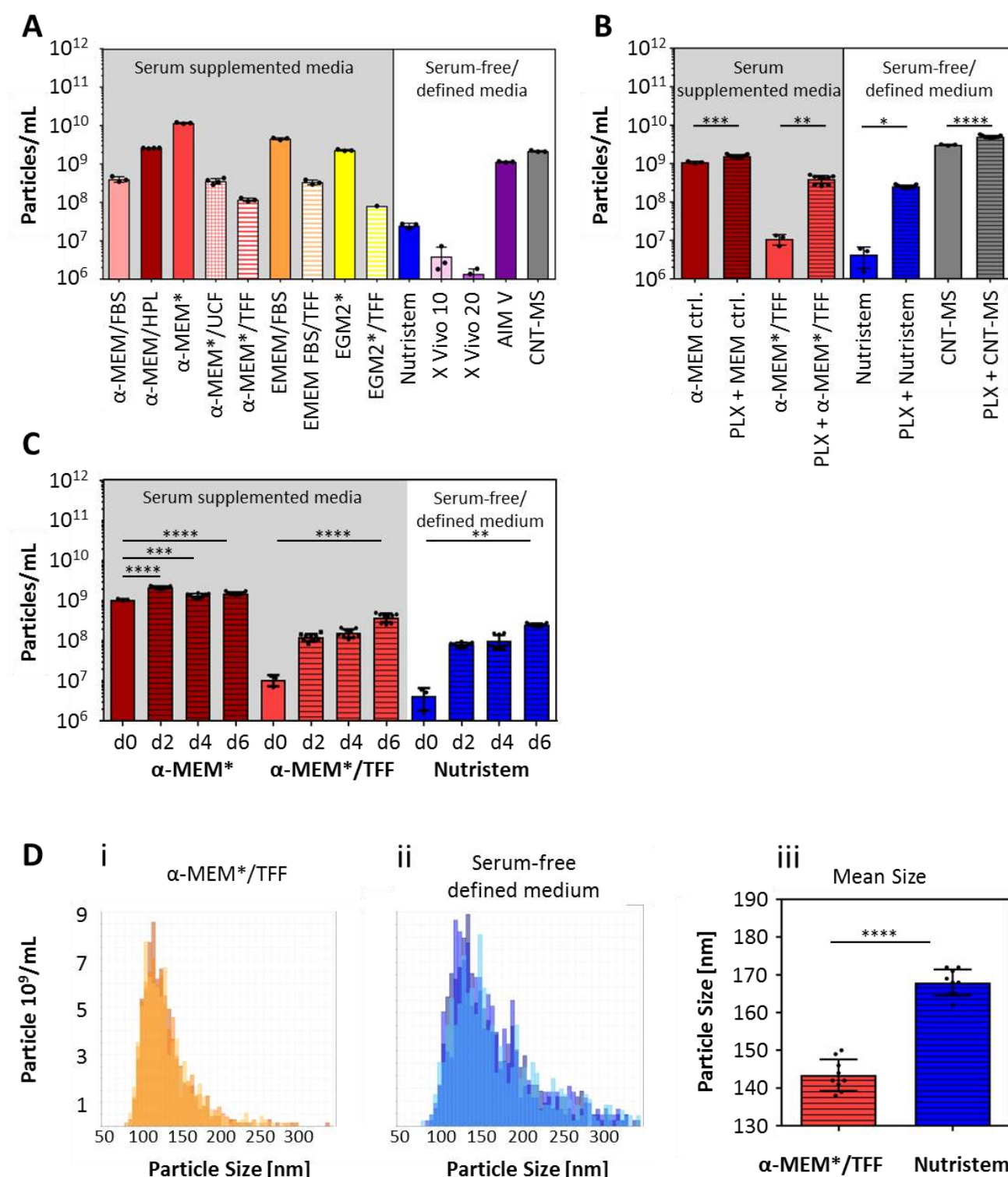
Figure S2: Physically defined media are required for cell-derived EV characterization. (**A**) Particle content of selected cell culture media with (left) or without serum (right) was measured by tunable resistive pulse sensing (TRPS). Media details are given in the methods section. (**B**) Comparison of the particle count in fresh and conditioned media after six-day placental stromal cell culture (PLX+). Particle concentrations were measured from three independent donors in four different media. (**C**) Time course of EV production in α-MEM*/TFF (*see Fig.1*) was compared to serum free defined medium. TRPS analysis was performed for three independent donors in triplicates over six days. (**D**) TRPS

measurement of PLX stromal cell-secreted EVs showed (**iii**) significantly different particle size distribution in (**ii**) defined serum-free vs. (**i**) platelet lysate-supplemented media (TFF pre-depleted). Triplicate measurements from one representative donor are shown (i, ii). Data from three donors were analyzed statistically (iii).

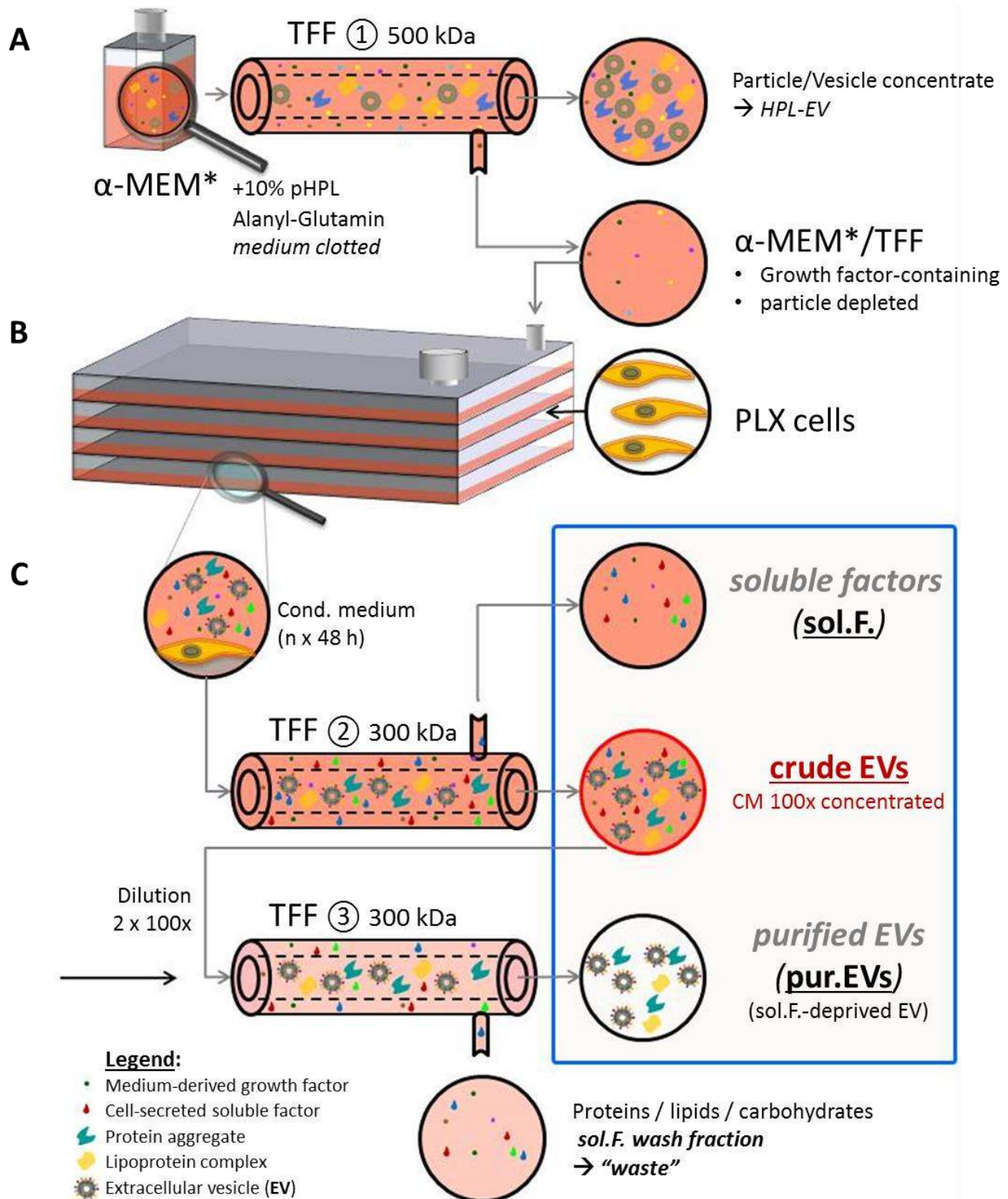**Figure 1: Schematic workflow of large-scale EV production from PLX cells.** (**A**) Cell culture medium α-MEM was supplemented with 10% pooled human platelet lysate (HPL)

October 17, 2019

and fibrinogen-depleted, as described, before further use (α-MEM*). To produce particle-free medium by tangential flow filtration (TFF; α-MEM*/TFF) for EV harvest, α-MEM* was filtered through a 500 kDa cut-off membrane. (**B**) 70% confluent PLX cells were cultured in particle free α-MEM*/TFF for one to three 48 h periods to obtain conditioned medium (CM). (**C**) Particles were enriched 100-fold by concentration in the TFF system (crude EVs) and separated from soluble factors (sol. F.). To remove remaining soluble factors/proteins, this crude concentrate was washed with twice the initial start volume to yield purified EVs separated from soluble factors.

Transmission electron microscopy showed typical appearance of round shaped vesicles of about 100 nm size with negative staining (**Fig.2A**) and characteristic double membrane-surrounded vesicles in high-resolution cryo-electron microscopy images that showed more protein background in crude EV and less in purified EV preparations, respectively (**Fig.2BC**).
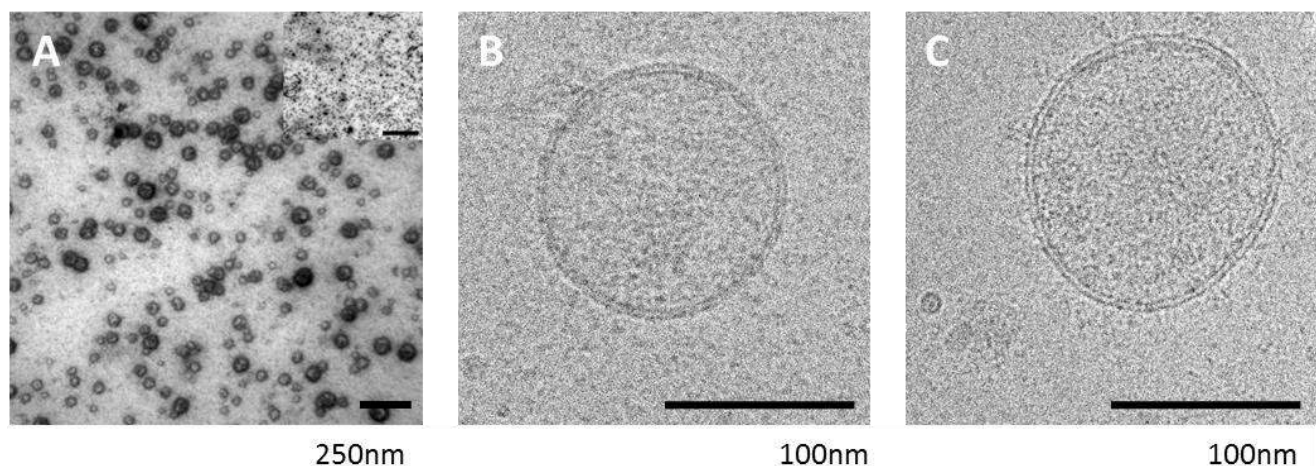
Figure 2: Crude vs. purified PLX cell-derived EV characterization. (**A**) Transmission electron microscopy image of PLX-EVs with negative contrast. (**B**) Cryo-TEM pictures of highly magnified PLX-derived crude EVs and (**C**) purified EVs. Scale bar 250 nm (in **A**) and 100 nm (in **BC**). Lower magnification overview insert scale bar 1000 nm (in (**A**).

Western blots to further characterize EV identity for providing information for studies of extracellular vesicles [9] showed comparably high CD81 and lower CD9 tetraspanin expression levels in three representative purified EV preparations from PLX cells of three individual placentas. Lineage specificity of tetraspanin expression levels was supported by direct comparison to endothelial progenitor cell-derived lower CD81 and higher CD9 levels (**Fig.3A**). Loading corresponding amounts of protein resulted in a significantly enhanced signal for all three EV associated tetraspanins tested in purified as compared to crude EV preparations. The membrane raft marker flotillin-1 was found to be significantly enriched in purified EVs compared to crude EVs.

8

Figure 3: EV identity and purity determined by western blot. (**A**) Identity confirmation for EVs from three individual PLX donors (Lots P15, P25, P27) compared to one endothelial colony-forming progenitor cell (ECFC) preparation showing lineage specific tetraspanin

9
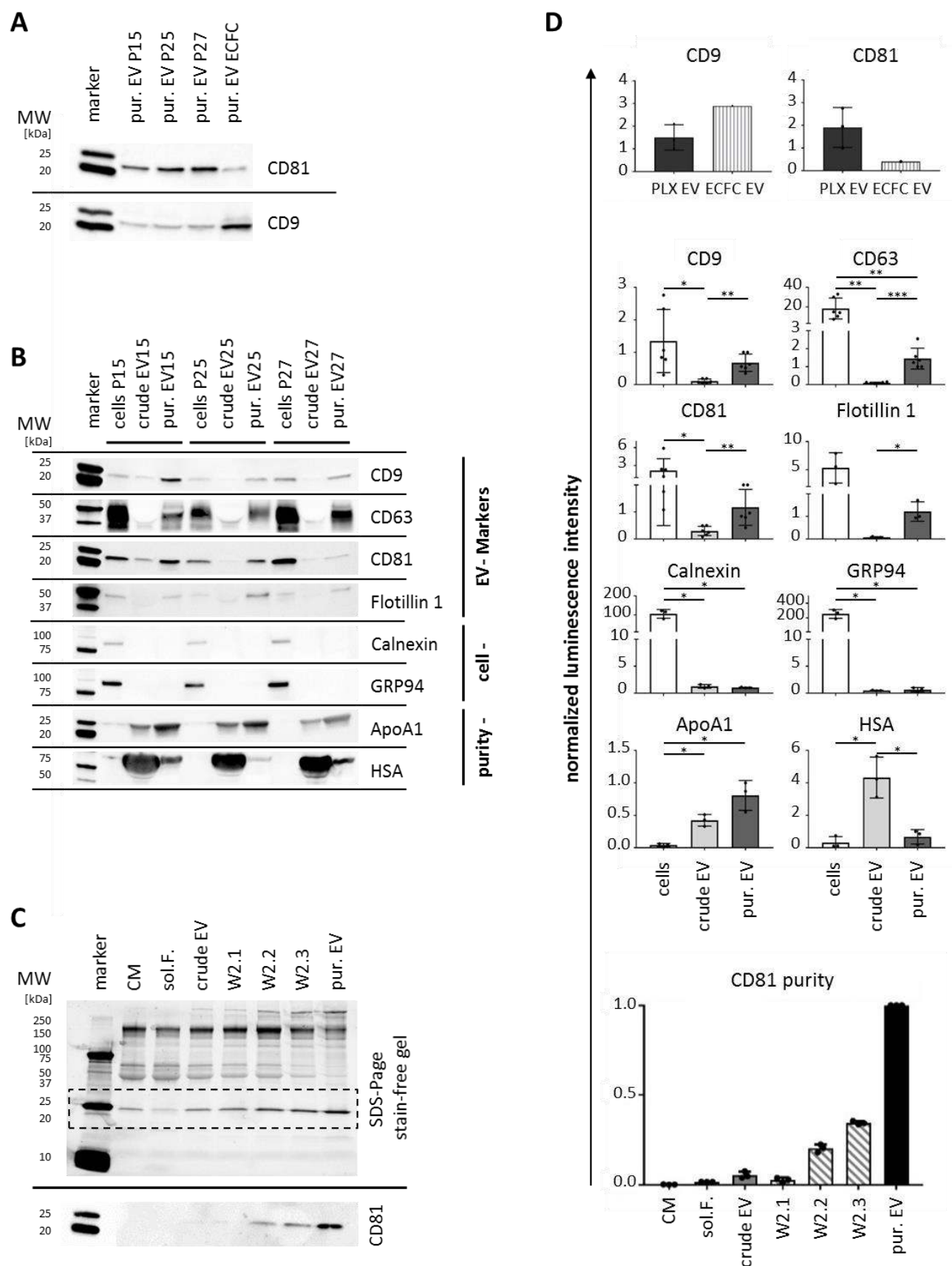
CD81 and CD9 differences. (**B**) Comparing parental PLX cells (from the same lots P15, P25, P27 as shown in **A**) and corresponding EV preparations (crude EV and purified EV from PLX lots 15, 25 and 27, EV15, EV25 and EV27, respectively) for tetraspanins CD9, CD63, CD81, compartment specific markers flotillin, calnexin and GRP94, as well as apolipoprotein A1 (ApoA1) and human serum albumin (HSA). (**C**) Monitoring of protein and tetraspanin CD81 enrichment during the concentration and purification process. One representative preparation is shown of three tested. (**D**) Densitometric analysis of blots shown in **A**-**C** normalized to total protein/lane. Significant differences (*p < 0.0332, **p < 0.0021 and ***p < 0.0002) were identified based on two-tailed t-test with 95% confidence level. The complete western blot membranes are shown in a comprehensive **Fig. S8**.

The endoplasmic reticulum lectin, calnexin, and the golgi membrane stacking protein, GRP94 were found to be present only in cell-derived protein preparations as to be expected (**Fig.3BD**). To assess the purity of EV preparations we probed for apolipoprotein A1 (Apo A1) as a marker for lipoproteins and human serum albumin (HSA) as a contaminating protein highly abundant in culture medium. We found an efficient depletion of HSA during the second TFF purification step and significant enrichment of Apo A1 in purified EVs. Questioning the performance of our EV purification procedure, we found a continuous enrichment of a 25 kDa protein band throughout the whole purification process (**Fig.3C top**), that was confirmed to represent CD81 after blotting and immunostaining (**Fig.3C bottom**). Densitometric analysis of the EV preparations from three independent donors revealed enrichment of EV specific markers, absence of cell-compartment specific proteins and efficient depletion of soluble protein as indicated by reduced HSA levels in purified EVs (**Fig.3D**).

Using multiplex bead-based flow cytometry [23] for EV surface marker profiling of three independent purified PLX-EV preparations confirmed high expression of tetraspanins CD81/CD63 and reduced CD9 expression. We found medium classified expression of the fibronectin receptor CD49e/CD29 and high/medium expression of the extracellular matrix interaction molecules CD44 and NG2 as well as the cytokine receptor CD105 (endoglin) and CD142 (coagulation factor III, tissue factor). The majority of hematopoiesis marker molecules displayed in this assay were confirmed to be absent on purified PLX-derived EVs (**Fig.4A**).

10

October 17, 2019
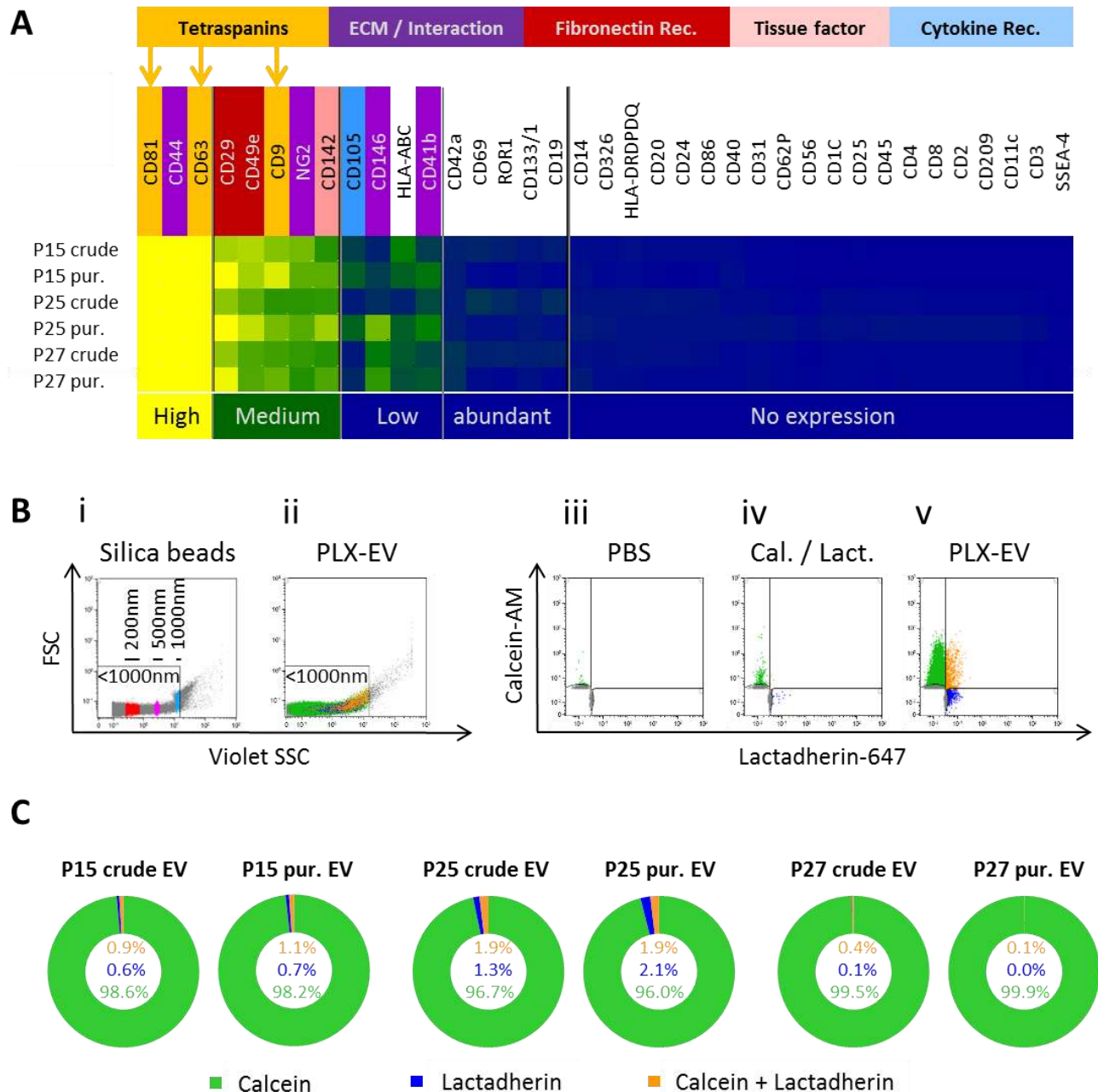
Figure 4: Antibody-based EV marker profiling indicated distinct address code and low abundance of apoptotic bodies. (**A**) Heat map showing mean surface marker expression of crude vs. purified (pur.) PLX-EVs from three individual donors (P15, P25, P27) as determined by bead-based multiplex flow cytometry (MACSPlex). (**B, i**) Fluorescent silica beads (Kisker) were used to adjust small particle resolution in flow cytometry and to set a size gate <1000 nm for EV detection. (**B, ii**) Dot plot showing size distribution of a representative PLX-EV sample. (**B, iii**) Dot plots showing fluorescence background of unstained PBS control, (**B, iv**) calcein-AM and lactadherin-Alexa Fluor 647 stained PBS control without EVs added (Cal. / Lact.) and (**B, v**) representative double-stained PLX-EV plot showing the distribution of calcein[+] and lactadherin[+] events using a dual fluorescence trigger. (**C**) Determination of calcein[+] EVs and lactadherin[+] presumably apoptotic bodies in crude vs. purified PLX-EV preparations, depicted as pie chart of marker distribution of the positive events. Negative events were excluded from analysis because current technology does not permit precise discrimination between electronic noise and non-fluorescent

11

unstained EVs or other undetermined non-particulate non-fluorescent signals notably in the size range of 100 nm and below [24].

After establishing flow cytometry instrument sensitivity based on silica size marker beads we defined a gating strategy to enable measurement of nano-particles (sized between >100 nm up to <1000 nm). Negative control phosphate buffered saline (PBS) with and w/o calcein and lactadherin reagents, respectively, showed only minute unspecific reactivity (**Fig.4Biii & iv**). Flow cytometry of crude vs. purified EV preparations showed predominantly calcein converting EVs (**Fig.S3 and Fig.4Bv**). Distribution of calcein and lactadherin fluorescence-triggered events for each EV preparation indicated that ≥ 96% of detected EVs were derived from intact cells (calcein single positive) and presumably not apoptotic bodies (lactadherin negative). By back-gating lactadherin and calcein double-positive events in the size gate (**Fig.4Bii**, PLX EV plot), the estimated apoptotic bodies were more apparent in the 500 – 1000 nm size range as described in the literature [25] (**Fig.4C**).
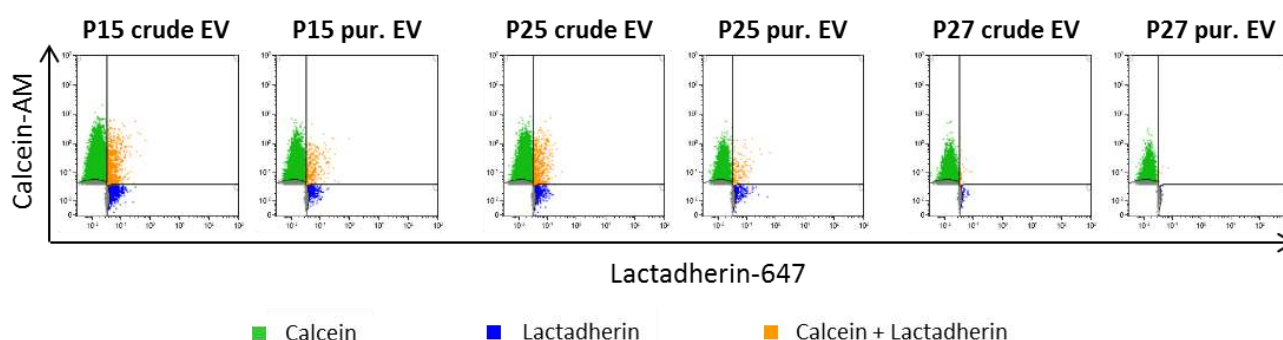
Figure S3: Crude vs. purified EV flow cytometry. Dual fluorescence triggering-derived dot plots based on the gating strategy shown in Fig.4B was used to determine the number of calcein+ EVs and lactadherin+ presumably apoptotic bodies in three independent pairs of crude vs. purified PLX-EV preparations from PLX cultures of placenta lots P15, P25 and P27, respectively. Corresponding pie charts are depicted in Fig.4C.

The EV purification protocol devised in this study allows for efficient high throughput separation of soluble factors from EVs out of the otherwise protein-contaminated crude EV fraction after sequential TFF enrichment of CM preparations (illustrated in **Fig.5A**).

Targeted proteomic pre-analysis using western blot-based arrays for comparing unconditioned cell culture media vs. soluble factor fractions (derived from CM) and crude

October 17, 2019

vs. purified PLX-EVs revealed measurable differences between the four fractions (**Fig.S4A**).
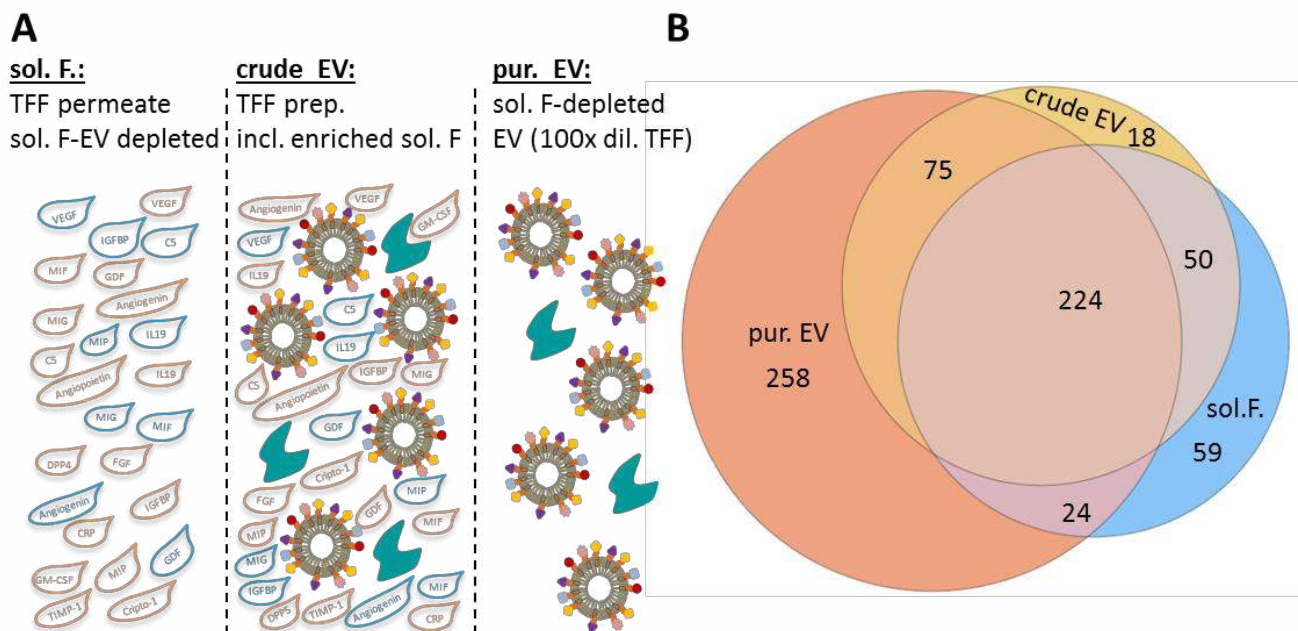
Figure 5: Proteomic composition of PLX secretome fractions. (**A**) Illustration of different fractions separated by TFF. A graphic symbol legend is shown in Figure 1. (**B**) Venn diagram showing the overlap and differences in proteins identified by label-free proteome analysis in the different secretome fractions (soluble factors, sol.F.; crude EV; purified EV, pur. EV) from three donors in two independent experiments.

The majority of highly abundant proangiogenic factors was found to be present in both, crude and purified EVs. We did not find specific factors to be significantly enriched in purified EVs over crude EV, using this technology (**Fig.S4B**).

October 17, 2019

A

α-MEM*   sol. F.   crude EV   pur. EV

B

Proangiogenic factors	α-MEM*	sol. F.	crude EV	pur. EV
Serpin E1 PAI-1	0,230	0,675	0,730	
Platelet Factor 4 (PF4) CXCL4	0,563	0,355	0,757	0,787
Thrombospondin-1 /TSP-1	0,358	0,139	0,669	0,599
Serpin F1 PEDF	0,472	0,486	0,355	0,358
Coagulation Factor III (TF) (CD142)	0,001	0,001	0,699	0,613
Pentraxin 3 (PTX3) TSG-14	0,001	0,005	0,225	0,261
Angiopoietin-1	0,013	0,001	0,363	0,244
Endoglin (CD105)	-0,001	0,000	0,243	0,181
uPA	0,001	0,122	0,397	0,225
DPP IV/CD26	0,079	0,002	0,798	0,652
IGFBP-3	0,134	0,020	0,367	0,160
TIMP-1	0,037	0,353		0,011
Angiogenin	0,203	0,204	0,562	0,036
IGFBP-1	0,005	0,007	0,090	0,006
IGFBP-2	0,003	0,005	0,070	0,003
MMP-9	0,003	0,006	0,050	0,016
HGF	0,001	0,002	0,026	0,006
Serpin B5 Maspin	0,008	0,011	0,002	0,025
Angiopoietin-2	0,033	0,045	0,011	0,041

Figure S4: Proteomic characterization of PLX secretome fractions. (**A**) Antibody array-based analysis of proangiogenic factors in the different secretome fra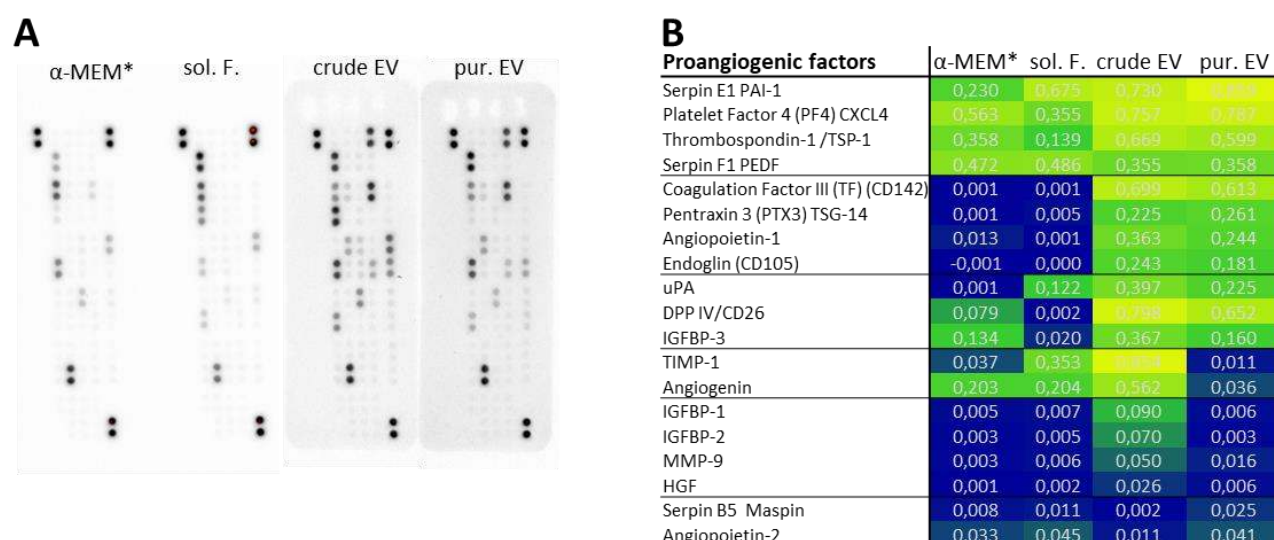ctions (derived from one representative donor). (**B**) Heat map representation of corresponding quantitative analysis of PLX secretome fractions as indicated. Numbers represent relative luminescence units.

We therefore performed a more detailed proteome analysis using two different approaches. We analyzed the protein composition of soluble factors, crude and purified EVs compared to unconditioned media to identify proteins uniquely present in the different fractions by qualitative label-free proteomics. Pre-analytics confirmed depletion of total protein content from crude EVs in the purified EV fractions by the factor of 4.87 – 18.33 accompanied by a further enrichment of EVs by the factor of 1.34 – 3.30. A total of 401 - 1,168 proteins was detected in the different donor-derived fractions analyzed by label-free proteomics. (**Table S1**). Only proteins detected in the corresponding fractions of at least two different donors (708 proteins in total) were selected for further analysis. We could identify 258 proteins that were uniquely present in purified EVs. Many of these proteins were related to either cell movement, adhesion, immune system regulation or angiogenesis (**Table S2**). Furthermore, 59 proteins unique to the soluble factors and 18 proteins enriched in the crude EVs were found; 224 proteins were present in all three fractions. (**Fig. 5**).

To get deeper insights into differentially expressed proteins present in all fractions, we used differential proteomics with tandem mass tag (TMT) labels in the different secretome fractions from three independent donors. Due to higher sensitivity of the TMT method, we could detect 1115 proteins differentially expressed in all fractions. Heatmap analysis of the

October 17, 2019

different secretome fractions revealed a distinct pattern of protein clusters present in every fraction (**Fig. 6A**). Volcano plot showing statistical analysis of fold change in proteins differentially represented in purified EVs vs. soluble factors. Significantly different proteins were identified to be key molecules involved in immune response modulation, angiogenesis and cell movement together with EV marker molecules and were over-represented in the purified EV fraction. These proteins were highlighted according to selected corresponding GO terms as listed in table S2. (**Fig. 6BC; Table S2; Fig. S5**). Ingenuity pathway analysis revealed several canonical signaling pathways differentially over-represented among proteins in EV preparations compared to the soluble factor fraction (**Fig. S6A**). Multiple disease and functional categories related to cell angiogenesis, movement and the immune response were also classified to be enriched in the EV proteome (**Fig. S6B**).
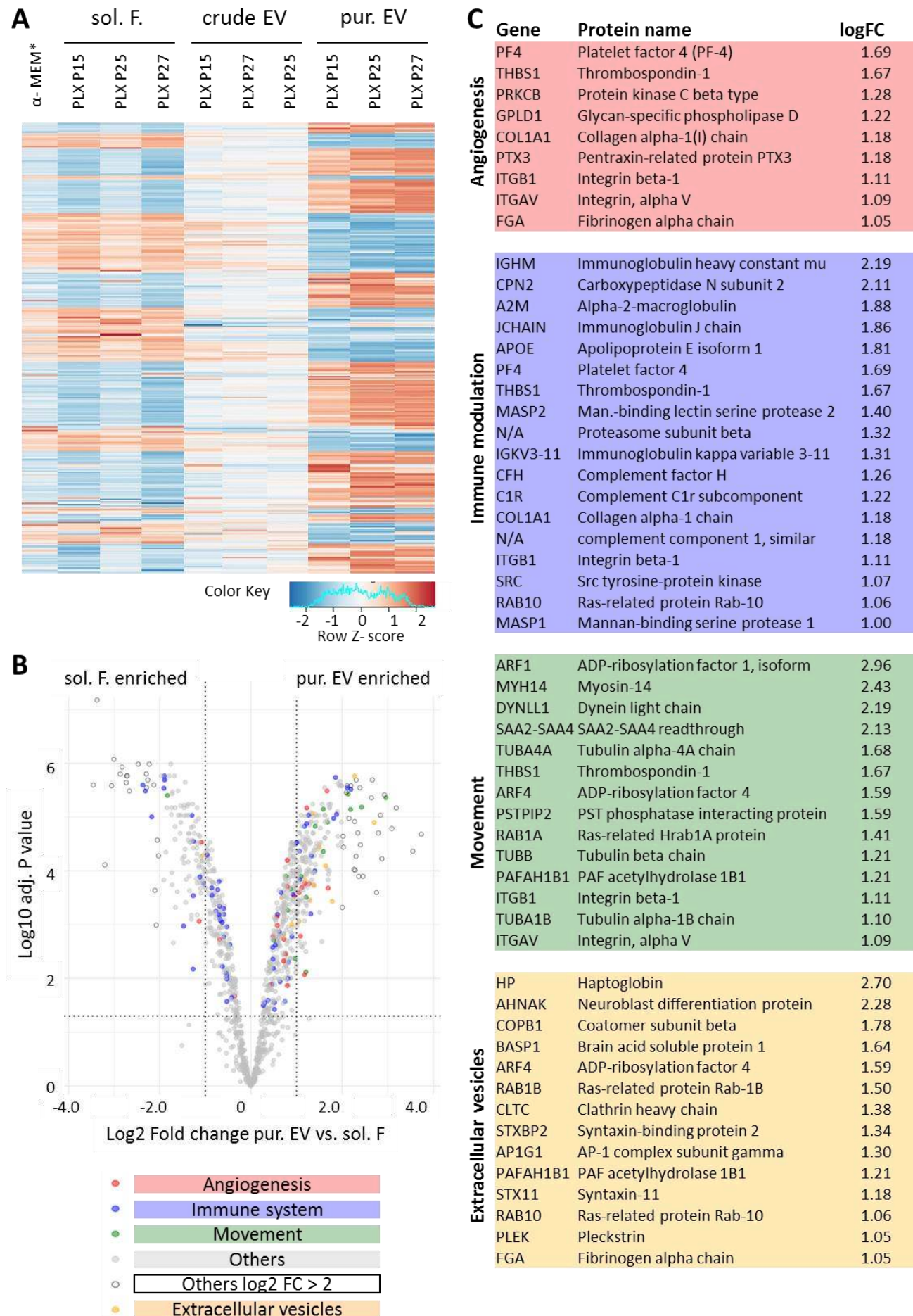
15

A

B

C

	Gene	Protein name	logFC
Angiogenesis	PF4	Platelet factor 4 (PF-4)	1.69
	THBS1	Thrombospondin-1	1.67
	PRKCB	Protein kinase C beta type	1.28
	GPLD1	Glycan-specific phospholipase D	1.22
	COL1A1	Collagen alpha-1(I) chain	1.18
	PTX3	Pentraxin-related protein PTX3	1.18
	ITGB1	Integrin beta-1	1.11
	ITGAV	Integrin, alpha V	1.09
	FGA	Fibrinogen alpha chain	1.05

	Gene	Protein name	logFC
Immune modulation	IGHM	Immunoglobulin heavy constant mu	2.19
	CPN2	Carboxypeptidase N subunit 2	2.11
	A2M	Alpha-2-macroglobulin	1.88
	JCHAIN	Immunoglobulin J chain	1.86
	APOE	Apolipoprotein E isoform 1	1.81
	PF4	Platelet factor 4	1.69
	THBS1	Thrombospondin-1	1.67
	MASP2	Man.-binding lectin serine protease 2	1.40
	N/A	Proteasome subunit beta	1.32
	IGKV3-11	Immunoglobulin kappa variable 3-11	1.31
	CFH	Complement factor H	1.26
	C1R	Complement C1r subcomponent	1.22
	COL1A1	Collagen alpha-1 chain	1.18
	N/A	complement component 1, similar	1.18
	ITGB1	Integrin beta-1	1.11
	SRC	Src tyrosine-protein kinase	1.07
	RAB10	Ras-related protein Rab-10	1.06
	MASP1	Mannan-binding serine protease 1	1.00

	Gene	Protein name	logFC
Movement	ARF1	ADP-ribosylation factor 1, isoform	2.96
	MYH14	Myosin-14	2.43
	DYNLL1	Dynein light chain	2.19
	SAA2-SAA4	SAA2-SAA4 readthrough	2.13
	TUBA4A	Tubulin alpha-4A chain	1.68
	THBS1	Thrombospondin-1	1.67
	ARF4	ADP-ribosylation factor 4	1.59
	PSTPIP2	PST phosphatase interacting protein	1.59
	RAB1A	Ras-related Hrab1A protein	1.41
	TUBB	Tubulin beta chain	1.21
	PAFAH1B1	PAF acetylhydrolase 1B1	1.21
	ITGB1	Integrin beta-1	1.11
	TUBA1B	Tubulin alpha-1B chain	1.10
	ITGAV	Integrin, alpha V	1.09

	Gene	Protein name	logFC
Extracellular vesicles	HP	Haptoglobin	2.70
	AHNAK	Neuroblast differentiation protein	2.28
	COPB1	Coatomer subunit beta	1.78
	BASP1	Brain acid soluble protein 1	1.64
	ARF4	ADP-ribosylation factor 4	1.59
	RAB1B	Ras-related protein Rab-1B	1.50
	CLTC	Clathrin heavy chain	1.38
	STXBP2	Syntaxin-binding protein 2	1.34
	AP1G1	AP-1 complex subunit gamma	1.30
	PAFAH1B1	PAF acetylhydrolase 1B1	1.21
	STX11	Syntaxin-11	1.18
	RAB10	Ras-related protein Rab-10	1.06
	PLEK	Pleckstrin	1.05
	FGA	Fibrinogen alpha chain	1.05

16

Figure 6: Quantitative proteomic characterization of PLX cell secretome fractions. (**A**) Heatmap comparing the proteome of soluble factor fractions (sol. F.), crude EVs and purified (pur.) PLX-EVs with human platelet lysate-supplemented defibrinized unconditioned cell culture medium (α-MEM*/TFF). (**B**) Volcano plot comparing protein expression signal significance to levels of enrichment in sol. F. vs. pur. EV. Functional categories according to corresponding GO terms as listed in **Table 2** are depicted as color coded dots as indicated; additional highly over-represented proteins marked as open circles (see also **Figure S6**). (**C**) Selected proteins most predominantly over-represented in pur. EVs. Color code corresponding to (**B**). Complete proteomics data have been uploaded to PRIDE [accession N°.: PXD014572]

As a functional readout validating our proteomic results, we analyzed the different vesicular and soluble PLX secretome fractions for their capacity to stimulate endothelial network formation on matrigel as an *in vitro* test for angiogenic potential. We found that crude EVs as well as purified EVs and soluble factors induced supra-maximum network formation of endothelial colony-forming progenitor cells (ECFCs) compared to complete angiogenesis-supportive medium positive control in a 10,000:1 ratio. Crude EVs had significantly higher angiogenic potential than purified EVs for the 1000:1 and 100:1 ratio and compared to soluble factors in the 100:1 ratio only, indicating proangiogenic potential of both EVs and soluble factors (**Fig. 7A**). As a second readout, we tested the potential of the different PLX secretome fractions compared to PLX cells to inhibit mitogen-driven vs. allogenic mixed leukocyte reaction (MLR)-induced T cell proliferation. PLX cells significantly inhibited both mitogen-induced as well as allogeneic T cell proliferation in a dose dependent manner with reaching almost 100% inhibition at a PLX cell-to-PBMC ratio of 1:1. Crude EVs were as effective in inhibiting mitogen-induced T cell proliferation in a 15,000:1 ratio. Purified EVs had a significantly reduced capacity to inhibit T cell proliferation at lower ratio. Surprisingly, PLX-derived soluble factors did not affect T-cell mitogenesis in this assay (**Fig. 7C**). Interestingly purified EVs had no inhibitory effect on the MLR response at higher ratio and even showed a slight boost of the T cell proliferation like the PLX cells at lowest concentrations (**Fig. 7D**).
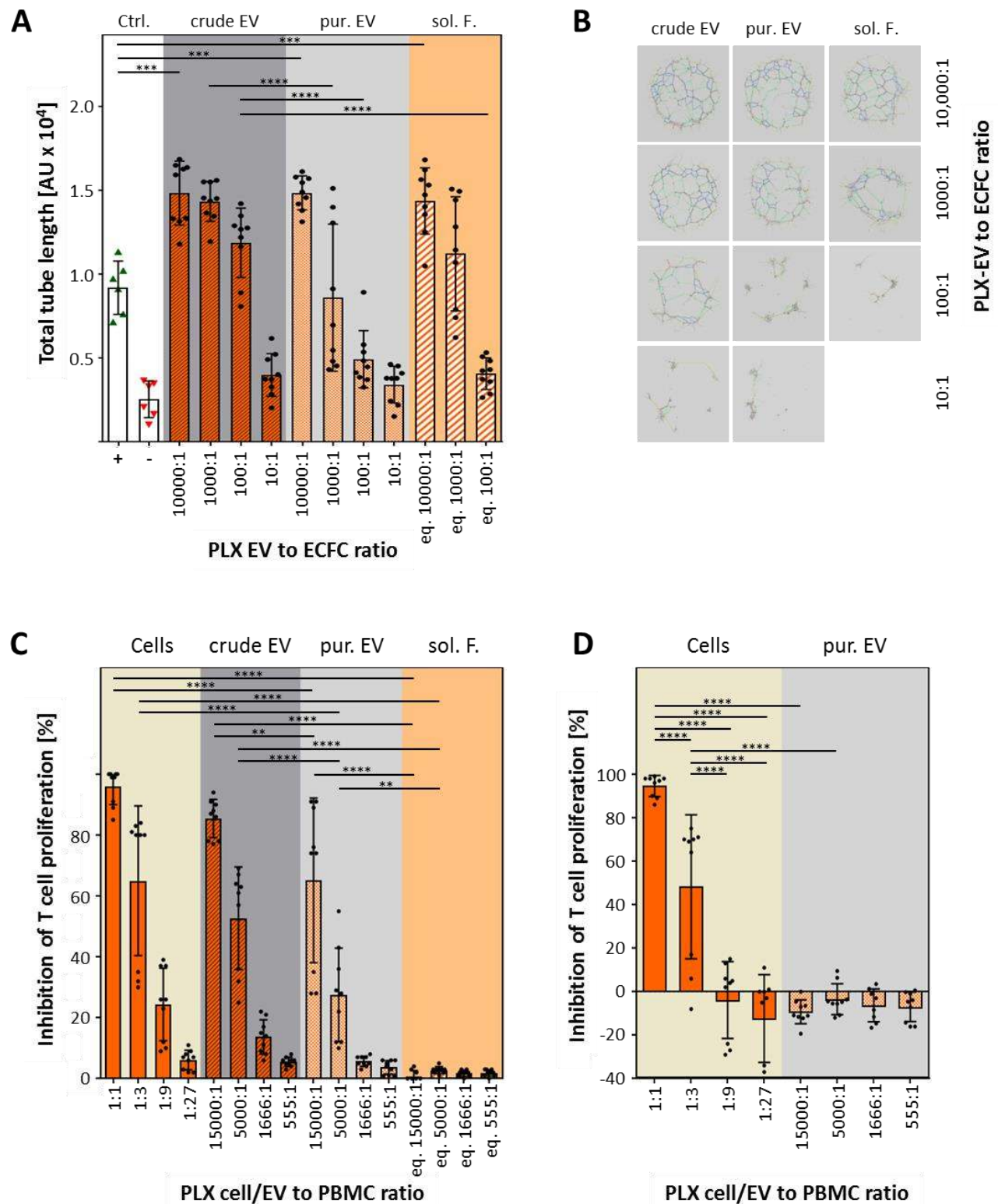
October 17, 2019

Figure 7: Angiogenic and immunomodulation potential of EVs: **(A)** Angiogenic potential of different PLX secretome fractions was analyzed by endothelial network formation in a matrigel assay. Total length of the endothelial colony-forming progenitor cell (ECFC) networks in the presence of crude or purified PLX-EVs at the indicated EV:ECFC ratio is shown. Volumes of soluble factors (sol. F.) added to the assay were calculated accordingly corresponding to the EV numbers as described in the methods section. Results were pooled from three independent donors (***p < 0.0002, ****p < 0.0001). **(B)**

October 17, 2019

Representative pictures of ECFC networks in the matrigel assay shown in A. (**C**) Immunomodulation by PLX secretome fractions was measured by their capacity to inhibit PHA-induced T cell proliferation. The percentage of inhibition was calculated relative to the maximum proliferation induced by PHA. Pooled results of three independent donors measured at day four (**p < 0.0021, ***p < 0.0002, ****p < 0.0001). (**D**) Comparison of PLX cells and purified PLX-EVs for their capacity to inhibit allogeneic T-cell proliferation in a mixed leukocyte reaction measured at day seven (**p < 0.0021, ***p < 0.0002, ****p < 0.0001).

DISCUSSION

In this study, we devised an efficient isolation and purification strategy suitable for mass-production of EVs for high-content proteomic and functional analysis. Based on previously established large-scale cell propagation protocols [22], [26], [27], up to one trillion purified EVs could be obtained from one liter of CM within less than a working day (e.g. 5mL final TFF concentrate including 2×10^{11} EVs/mL). TFF depletion of starting media or the use of defined particle-free media permits directed cell-derived EV analysis devoid of serum- or culture supplement-derived EV or particle contamination [28]. EV identity and purity achieved with this strategy was confirmed by western blot and flow cytometry according to MISEV 2018 criteria [9].

The efficacy of PLX cells for the treatment of CLI is currently evaluated in a randomized, double-blind, multicenter, placebo controlled phase III clinical trial based on preclinical data indicating systemic activity of soluble factors secreted by the PLX cells and based on a favorable safety profile in two phase I studies [1], [2]. Taking advantage of the straightforward separation of soluble factors from EVs out of conditioned media by stepwise TFF (**Fig. 1**), we focused in this study on in-depth proteomic analysis. We demonstrated that proteomes in soluble factor as compared to EV fractions significantly differ. Key angiogenic factors enriched in purified EVs included platelet factor-4, thrombospondin and integrins, among others (**Fig. 6C**) Despite these differences, both crude and purified PLX-EV fractions as well as the PLX cells induced supra-maximum vascular network formation in a dose dependent manner *in vitro*. This could be explained by the fact that several proteins involved in vascular remodeling (e.g. serpins, PF4, TSP-1 and angiogenin, **Fig. S4B**) were present in the soluble factor as well as EV preparations. Provided, that a comparable 'soluble factors plus EVs' secretome pattern also occurs in patients, our results

19

would indicate that PLX cell-derived EVs may be considered to contribute to the therapeutic effect in CLI. We may speculate that EVs can act over longer periods of time beyond rejection of the allogenic cells and degradation of secreted factors. A precise assignment of the various effects rendering different aspects of vascular remodeling and wound healing induced by PLX cells or their soluble and vesicular secretome fractions in CLI patients requires additional research that is currently underway in mechanistic side studies accompanying the ongoing clinical trial (http://www.pace-h2020.eu/).

We identified immunity in addition to angiogenesis as predominantly affected by pathways that require action of the proteins over-represented particularly in purified PLX-EVs. This comes not too surprising given the fact that PLX, like many other stromal cells, bear an immunomodulatory capacity, at least *in vitro* [4], [6]. In contrast to angiogenesis, an immune response modulation capacity as determined by inhibition of T cell mitogenesis in a dose-dependent manner was assigned only to the PLX cells and their EVs. In this assay, purified EV were significantly less efficient than crude EV and PLX cells. A more detailed subtractive analysis is currently underway to better delineate the still ill-defined immunological aspects of stromal cell-derived EV function. Immune response modulation by stromal cells and their cell-derived trophic factors so far has been viewed in a rather simplistic way as immune suppression, because standard readouts commonly measure inhibition of immune cell proliferation and effector function [6]. Evidence from sepsis models however favors the view of a peculiar immunomodulatory role of stromal cell therapy being capable of reducing sepsis mortality [29]. In a recent phase I dose escalation study for the treatment of sepsis by allogeneic bone marrow stromal cell infusion, no elevation of circulating cytokines was found [30]. This does not exclude the possibility that soluble stromal cell-derived factors or EVs act locally or that other factors not included in the test panel are involved, but it highlights the difficulty to obtain suitable biopsies for biomarker discovery and for studying the mode of action of therapeutic cells in vivo. It also tempts to speculate that EVs may be involved in immunomodulation also in sepsis.

The reduced efficacy of PLX cells at low input cell number (i.e. higher ratio) as inhibitors of the allogeneic MLR (**Fig. 7D**) is reminiscent of previous results with other stromal cell types [31], [32], and in accordance with the literature [6]. The complete lack of allogeneic MLR inhibition by PLX-EV may highlight the need for selecting particularly potent EVs and/or cells for the treatment of allo-immunity-related conditions, including graft-versus-host disease [33], [34]. We therefore plan a more detailed analysis, particularly of the immune-

October 17, 2019

related proteomic profile of EVs vs. donor cells vs. soluble factors, and validation of results in additional experimental models towards rational potency-based selection of cell- and EV-based therapeutics. This will include comprehensive genomic analysis focusing on small RNA species as initiated previously in a study for monitoring the immunomodulatory potential of neonatal umbilical cord stromal cell-derived EVs [18]. Our quantitative EV purification approach will also allow for combining lipidomics, glycomics and metabolomics for a more broad view on PLX-EV biology using upcoming technology [35]–[37]. EV characterization can not be limited to key pathways of angiogenesis and immunity. Tissue factor, which has been described to limit hemocompatibility and thus hamper systemic transplantability of hepatocytes and Langerhans' islets [38], was detected at moderate levels on the PLX-EV surface in this study. Initial experiments already showed a significant procoagulant capacity of PLX cells and their crude as well as purified vesicles arguing in favor of a safe local administration (**Fig. S7**). In particular for systemic applications, selection of products with sufficient hemocompatibility due to low/absent tissue factor expression or lack of complement activation may be beneficial as described for cell transplants [39]. Results obtained in these studies might have an impact on future protocols for EV manufacturing [40].

This study has certain limitations. The precise position of EV-associated proteins inside vesicles as compared to a location in a protein corona adjacent to the vesicles still needs to be determined. The continuous enrichment of EV marker molecules (observed with each TFF washing step as observed in western blots, **Fig. 3C**) and the up to 18-fold reduction of protein contamination throughout the purification process argue in favor of our protocol. Reaching a higher level of purity is expected to result in more precise information from future high content omics screening. Understanding the relative contribution of cells vs. soluble factors vs. EVs to therapeutic efficacy and monitoring the fate particularly of EVs in vivo will be a major challenge on the way towards rational design of efficient cell- and EV-based therapies [8], [12].

MATERIALS & METHODS

All materials and methods used in this study are summarized in detail in the online section.

21

October 17, 2019

ONLINE METHODS SECTION

Cell culture media and reagents

Serum- or plasma-containing media tested in this study included α-MEM, Eagle's MEM (EMEM, both Sigma- Aldrich, USA) and endothelial growth medium (EGM2, Lonza, USA). Media were supplemented with 10% pooled HPL or FBS as indicated, 5 mM N(2)-L-Alanyl-L-Glutamin (Dipeptiven, Fresenius Kabi, Austria) in the absence or presence of 2 U/mL preservative-free heparin (Biochrom, Germany) without antibiotics or with 100 U/mL penicillin and 0.1 mg/mL streptomycin (both Sigma-Aldrich, USA) as indicated in the results section. For ECFC culture EGM-2 was supplemented with hydrocortisone, hFGF, VEGF, IGF, EGF and ascorbic acid from the supplied bullet Kit (all Lonza) and FBS was replaced by an equivalent volume of pHPL [26], [41]. For particle depletion media were prepared by clotting supplemented α-MEM as described without heparin to avoid possible inhibition of EV function [15], [18], [19], [27], [42]. The collapsed fibrin clot was removed by centrifugation for 10 min, 3000 x g at room temperature. The resulting precleared medium was filtered through a 0.22 µm stericup filter (Merck Millipore, USA) and finally particle depleted using a 1,600 cm² 500 kDa cut off hollow fiber modified polyethersulfone (mPES) membrane filter column operated on a KR2i TFF System (Repligen, USA).This medium was termed α-MEM*/TFF. For comparison to TFF, we used ultracentrifugation that was performed at 100,000 x g for 3h in a Sorval WX80 ultracentrifuge with an T-865 rotor (both Thermo scientific, USA) as indicated.

Chemically defined and serum-free media included CNT-Prime (CELLnTEC, CH), X-Vivo-10, -15 and -20 (Lonza, USA) and MSC NutriStem XF medium (including a proprietary supplement mix; Biological Industries, Israel). Media were 0.22 µm sterile filtered prior to use.

PLX cell culture

Cryopreserved clinical grade PLX cell aliquots were obtained from Pluristem Inc. (Israel) as part of a European funded research project (http://www.pace-h2020.eu/). For this study, we used PLX cells derived from three individual donors, P150216R01, P250416R05 and P270114R27 (termed P15, P25 and P27, respectively). For EV production aliquots of 2.5

22

million PLX cells were propagated for one to two passages to avoid excess proliferation at moderate seeding density of 1,000 cells/cm² in 2,528 cm² cell factories (CF4, Thermo Fisher Scientific, USA) as established previously until approximately 70% confluence [19], [43]. For EV harvest PLX cells were washed twice with 37°C pre-warmed Dulbecco's PBS (Sigma Aldrich, USA) and cultured for an additional 48 h in particle depleted α-MEM*/TFF.

EV quantification

We used TRPS to quantify the particle content in various samples including fresh cell culture media, conditioned media, crude and purified EV preparations. Samples were diluted at least 1:1 in Dulbecco's PBS containing 0.05% Tween 20 that was also used as measurement electrolyte. Measurements were performed using a qNano Gold (Izon, New Zeeland) equipped with an NP150 nano-pore for the size range between 70 and 420 nm.

EV enrichment and purification

To isolate and purify EVs from PLX cells cultured in particle depleted medium, the conditioned medium was harvested after 48 h intervals. First, cells were depleted by centrifugation at 300 x g for 5 min followed by a 3,000 x g centrifugation step for 10 min to deplete cell debris. This precleared conditioned medium was first concentrated 100-fold using a 300 kDa cut off hollow fiber mPES membrane filter column operated on a KR2i TFF System (Repligen, USA). The particle-free soluble factor fraction was collected as permeate at this step while the crude EV preparation was kept as 'retentate' inside the system as illustrated in **Figure 1**. By washing this crude EV fraction with twice the starting volume NaCl 0.9% buffered with 10 mM HEPES an additional depletion of proteins and other non-vesicular non-particulate content was obtained resulting in the final purified EV fraction (**Fig.1**).

EV identity by western blot and flow cytometry

To analyze EV identity and purity aspects we performed western blotting using TGX stain free gradient 4-20% SDS- PAGE gels run in a mini-Protean system. Samples were loaded with Laemmli buffer containing 50 µM dithiothreitol (DTT), as reducing agent, except for tetraspanins CD9, 63 and 81. After transfer using the mini Trans-Blot tank system (all Bio-

Rad, USA), nitrocellulose membranes were probed with primary antibodies diluted in TBST with 2% BSA in the dilutions indicated in **Table S3**.

Detection was performed using horseradish peroxidase (HRP)-labeled secondary antibodies (rabbit anti-mouse IgG, A27025, Thermo Fisher, USA;, mouse anti-goat 205-035-108, Jackson Laboratories, USA; or polymer goat-anti-rabbit, K4002, DAKO EnVision, Agilent, USA) depending on the host species of the primary antibody and clarity enhanced chemiluminescence (ECL) substrate. Bands were visualized and quantified using a chemidoc system and image lab software (all Bio-Rad). Densitometry of specific bands was quantified after background correction in relation to the total protein content detected with the stain free technology before transfer as published [44].

In order to obtain a broader overview of markers present on the surface of PLX derived EVs we applied a bead-based screening assay measured with flow cytometry as described [45]. To standardize the EV input for the assay we loaded 1×10^9 EVs on the MACS Plex capture bead mix (Miltenyi, Germany)[23] stained with a mix of CD9-, CD63- and CD81-APC detection reagent mix according to manufacturer's protocol. Analysis was performed with an LSRFortessa instrument (BD, USA) equipped with 355 nm, 405 nm, 488 nm, 561 nm and 640 nm lasers. Raw measurement data were corrected for unspecific binding of the detection antibody mix to the beads and expressed as relative fold-change of mean fluorescence intensity (MFI) compared to samples stained with isotype control.

For single EV analysis by flow cytometry crude and purified PLX-EV preparations were stained with lactadherin-Alexa fluor 647 (CellSystems, Germany), and calcein AM (Sigma-Aldrich, USA) that were aggregate-depleted by centrifugation at 17,000 x g for 10 min directly prior to use. Staining with lactadherin was performed for 30 min at 4°C and subsequently, after 1:10 dilution of the samples, with calcein for 5 min at room temperature. Samples were further diluted 1:5 in PBS and analyzed on a Cytoflex flow cytometer (Beckman Coulter, USA). For creating a size-based gate <1000 nm for EV detection we used 100, 200, 500 and 1000 nm green fluorescent-labeled silica beads (Kisker Biotech, Germany) as illustrated in **Figure 4B** [46]–[48]. Based on the separation of fluorescent EVs from particle background we only recorded fluorescence-positive events using double fluorescence triggering in the FITC and APC channels. For quantifying calcein[+] and lactadherin[+] EV, gating was performed using staining reagents appropriately diluted in PBS as a negative control. Percentage of calcein, lactadherin and double-positive populations

October 17, 2019

was calculated as a part of the sum of all acquired events and were displayed as a pie chart (**Fig.4C**).

Electron microscopy

For conventional negative contrast transmission electron microscopy (TEM), 10 µL EV samples were applied on formvar-coated 100 mesh copper grids (Agar scientific, UK), fixed with 2,5% glutaraldehyde and stained with uranyl acetate replacement solution 1:10 (Electron Microscopic Sciences, UK) in bi-distilled water. Dried samples were imaged using an 80 kV LEO EM 910 transmission electron microscope (Zeiss, Germany) equipped with a Tröndle 227 Sharp Eye digital camera system. For cryo-TEM, EV samples were diluted 1:10 in 0,9% NaCl solution and 4 µl were applied to Quantifoil (Großlöbichau, Germany) Cu 400 mesh R1.2/1.3 holy carbon grids loaded a Cu 400 mesh R1.2/1.3 holy carbon grid (Leica Microsystems, Germany). Grids were glow discharged for 1 min at -25 mA with a Bal-Tec (Balzers, Liechtenstein) SCD005 glow discharger and loaded into a Leica GP grid plunger with the climate chamber set at 4ºC and 70% relative humidity. EV samples were diluted 1:10 in 0.9% NaCl solution and 4 µl were applied to the carbon side of the grid. After front-side blotting for 2 - 8 seconds (using the instrument's sensor function, no pre- or post-blotting incubation) with Whatman filter paper #1 (Little Chalfont, Great Britain) grids were plunge frozen into liquid ethane at approximately -180º C for instant vitrification. Cryo-samples were transferred to a Glacios cryo-transmission microscope (Thermo Scientific, USA) equipped with a X-FEG and a Falcon3 direct electron detector (4,096 x 4,096 pixels). The microscope was operated in a low-dose mode using the SerialEM software [49]. Images were recorded digitally in linear mode of the Falcon3 camera at magnifications of 5,300 (pixel size: 27.5 Å, defocus: -50 µm, dose: 0.2 e/Å2), 36,000 (pixel size: 4.1 Å, defocus: -6 µm, dose: 14 e/Å2) and 150,000 (pixel size: 0.98 Å, defocus: -3 µm, dose: 60 e/Å2).

Tandem mass tag proteomics (TMTP) and bioinformatics

Reagents included acetonitrile (≥ 99.9%) and methanol (≥ 99.9%; both VWR, Austria), DTT (≥ 99.5%), formic acid (98.0-100%), iodoacetamide (≥ 99.0%), sodium dodecyl sulfate

October 17, 2019

(SDS; ≥ 99.5%), triethyl ammonium bicarbonate (TEAB, 1 mol/L) and trifluoroacetic acid (≥ 99.0%; all Sigma-Aldrich, Austria), ortho-phosphoric acid (85%; Merck, USA), and sequencing grade modified trypsin (Promega, USA). Deionized water was purified with a MilliQ® Integral 3 instrument (Millipore, USA).

To determine protein content, samples were adjusted to 5% SDS and 50 mmol/L TEAB (pH 7.55) and incubated at 95°C for 10 min to lyse the EVs. Samples were analyzed by a Pierce™ bicinchoninic acid protein assay kit (Thermo Fisher Scientific, Austria) according to the manufacturer´s instructions. S-Trap™ mini columns (Protifi, Huntington, NY, USA) were utilized for sample preparation and 100 µg of protein were prepared according to the manufacturer´s instructions with minor adjustments: Lysis of EVs as well as denaturation and reduction of proteins were performed in 5% SDS and 50 mmol/L TEAB supplemented with 40 mM DTT at 95°C for 10 min. Cysteines were alkylated by the addition of IAA to a final concentration of 80 mM and incubated in the dark for 30 min. Proteins were digested within the S-Trap matrix with trypsin at an enzyme to substrate ratio of 1:10 w/w at 37°C for 18 h. Peptides were eluted and subsequently dried using a vacuum centrifuge. These samples were re-suspended in H_2O + 0.10% FA to a concentration of 3.33 mg/mL. Peptides of each sample (20 µg) were labeled by a TMT 10-plex™ kit (Thermo Fisher Scientific, Austria). Labeled samples were pooled and desalted using 100 µl Pierce™ C18 tips (Thermo Fisher Scientific, Austria) and dried again using a vacuum centrifuge. These samples were re-suspended in H_2O + 0.10% FA to a concentration of 5 mg/mL.

High-performance liquid chromatography (HPLC) separation was carried out on a nanoHPLC instrument (UltiMate™ U3000 RSLCnano, Thermo Scientific, Germany) at a flow rate of 300 nL/min and a column oven temperature of 50°C. Separation of unlabeled samples was performed on an Acclaim™ PepMap™ 100 C18 column (500 mm x 75 µm i.d., 3.0 µm particle size, Thermo Fisher Scientific, Austria). Samples (3.3 mg/mL; 0.15 µL) were injected using a microliter pick-up mode (loop volume 1 µL). A multi-step linear gradient of mobile phase solutions A (H_2O + 0.10% formic acid) and B (acetonitrile + 0.10% formic acid) was applied as follows: 1% - 22% B for 200 min, 22% - 30% B for 40 min, 30% - 55% for 30 min, 90% B for 20 min and 1% B for 40 min. Each sample was measured once.

Separation of TMT-labeled samples was performed on a 2000 mm µPAC™ C18 column (PharmaFluidics, Ghent, Belgium). The sample [5.0 mg/mL; 1µL] was injected using a microliter pick-up mode (5 µL loop volume). A multi-step linear gradient of mobile phase

October 17, 2019

solutions A and B was applied as follows: 1% - 22% B for 500 min, 22% - 40% B for 100 min, 90% B for 30 min and 1% B for 100 min. Five technical replicates were measured.

All mass spectrometry measurements were conducted in positive ion mode on a hybrid mass spectrometer (QExactive™ Plus benchtop quadrupole-Orbitrap® mass spectrometer) equipped with a Nanospray Flex™ ion source (both Thermo Scientific, Germany) and a SilicaTip™ emitter with 360 µm outer diameter, 20 µm inner diameter, and a 10 µm inner tip diameter (New Objective, Woburn, MA, USA). Mass spectrometric data were acquired with the following instrument settings: spray voltage of 1.5 kV, capillary temperature of 320°C, S-lens, radio frequency level 55.0, MS1 AGC target 3×10^6, m/z range 400-2000, maximum injection time of 100 ms, resolution of 70,000 at 200 m/z. Data-dependent tandem mass spectrometry (ddMS2) was carried out in the higher-energy collisional dissociation (HCD) cell at a normalized collision energy (NCE) setting of 28.0 and a resolution setting of 17,500 at m/z 200 for unlabeled samples and at a resolution of 35,000 at m/z 200 for TMT-labeled samples. For MS2, the top 15 signals were chosen for fragmentation with a 2.0 m/z isolation window, an automatic gain control target of 1^5 with a maximum injection time of 100 ms. The dynamic exclusion was set to 30 secons. The instrument was calibrated using Pierce™ LTQ Velos ESI Positive Ion Calibration Solution (Life Technologies, Vienna, Austria).

All data were evaluated using MaxQuant software (version 1.6.1.0) using default settings. A protein list was obtained from the Uniprot database including both Swiss-Prot as well as TrEMBL entries for homo sapiens (access: 10.03.2019) and was provided for MaxQuant searches [50], [51]. TMT-labeled data were further processed using Perseus software package (version 1.6.1.1)[52]. Only protein groups with 10 quantified channels were included for analysis, log2-transformed and normalized by subtraction of the median. Analysis of the TMT-labeled samples was conducted using Ingenuity® Pathway Analysis (IPA; version 47547484; Qiagen Bioinformatics, Redwood City. CA, USA).

R software (www.R-project.org) was used all further proteomics analysis. For the TMTP data, contaminants were removed and values were log2 transformed and normalized by subtraction of the median of each channel. In order to see how samples cluster together, a principle component analyses (PCA) and hierarchical clustering analysis using Euclidean distance were conducted on the whole normalized dataset. Then, we conducted differential expression analysis using limma package [53] and P-values were corrected using Benjamini and Hochberg multiple testing correction. Proteins were considered significantly

October 17, 2019

differentially expressed if the corrected Benjamini and Hochberg P-value was < 0.05 and absolute log2 fold change > 0.6. Data from the label-free proteomics analysis were used in order to detect proteins present in specific fractions. Samples were considered detected in a specific fraction if they were present in all 3 replicates. In order to estimate the biological process gene ontology (GO) terms enriched in the purified EV fraction, compared to the soluble factors, we combined the proteins that were significantly enriched in the EV fraction compared to the soluble factors (in the TMTP analysis) and/or found only in the EV fraction using the label-free proteomics analysis. Enrichment analysis was conducted using ClusterProfile R package [54] and GO were considered significantly enriched if the adjusted p-value was < 0.01 and the gene count was > 5. Only the most significantly enriched proteins were shown (fold enrichment > 4).

Angiogenesis, immunomodulation and thromboelastometry

To assay angiogenic potential of different PLX secretome fractions we used a vascular–like network formation assay on matrigel as previously described [55]. Umbilical cord blood (UCB)-derived ECFCs were seeded on top of matrigel (angiogenesis assay kit, Merck Millipore, USA) in an angiogenesis 96-well μ-plate (Ibidi, Germany) at a density of 31,500 cells/cm^2. Cells were treated with crude or purified EV preparations in an EV to ECFC ratio of 10,000:1, 1,000:1, 100:1 and 10:1 or with the volume equivalent of EV-free PLX stromal cell-derived soluble factors. Completely supplemented EGM-2 (Lonza) served as a positive control and unsupplemented EBM-2 as a negative control. Images were taken every hour for 12 hours on an Eclipse Ti inverted microscope (Nikon) equipped with a custom-build live cell incubation system (Oko Lab, Italy and Nikon, Austria) using a 4x objective. Images were processed with the NIS Elements Advanced Research package analysis software (Nikon). Total matrigel areas were cut out of raw images, homogenized (strength 16), and subjected to intensity equalization over XY. Afterwards, pictures were sharpened slightly and denoised (advanced denoising 5.0). Finally, lookuptables were adjusted to 3,000-13,000 and images were exported as TIFF files. Exported images were cut at the diameter of 1,300 pixels to remove edges of the plate and the contrast was enhanced. Processed pictures were analyzed to automatically detect the network structures with Image J using the Angiogenesis Analyzer plugin and total length of tube-like structures was determined (https://imagej.nih.gov/ij/macros/toolsets/Angiogenesis%20Analyzer.txt).

October 17, 2019

The effect of PLX-derived EVs on the immune response was analyzed using a T-cell proliferation assay as published earlier [18], [32]. In brief, peripheral blood mononuclear cells (PBMCs) were isolated and pooled from 10 individual donors before labelling with carboxyfluorescein succinimidylester (CSFE; Sigma- Aldrich, USA) and cryopreservation in appropriate aliquots for later use. These pre-labeled PBMCs (300,000 per flat bottomed 96-well plate) were than stimulated with 5 µg/mL phytohemagglutinin (PHA, Sigma- Aldrich, USA) to induce mitogenesis (at day four) or left untreated for seven days to monitor MLR responses. Assays were incubated with EVs dose dependently at three-fold serial dilution in a ratio of 15,000:1, 5,000:1, 1,666, or 555:1 for either four or seven days as indicated. The percentage of proliferating T cell was measured by flow cytometry as the fraction of viable CD3 positive cells with reduced CFSE staining compared to non PHA-stimulated cells. Inhibition of T cell proliferation was expressed as percentage relative to maximum proliferation without EV addition.

Thromboelastometry was determined in the absence or presence of one million PLX cells or one billion crude or purified PLX-EVs as recently described [39].

Statistics

Statistical analysis of the results was performed using One-Way ANOVA analysis of variance with a confidence interval of 95% and corrected for multiple comparisons using the Holm Sidak algorithm in GraphPad Prism version 7.03. Proteomic results were analyzed using R. A p value of <0.05 was defined as significant.

References:

[1]   L. Norgren *et al.*, "PLX-PAD Cell Treatment of Critical Limb Ischaemia: Rationale and Design of the PACE Trial," *Eur. J. Vasc. Endovasc. Surg.*, vol. 57, no. 4, pp. 538–545, Apr. 2019.

[2]   E. Zahavi-Goldstein *et al.*, "Placenta-derived PLX-PAD mesenchymal-like stromal cells are efficacious in rescuing blood flow in hind limb ischemia mouse model by a dose- and site-dependent mechanism of action," *Cytotherapy*, vol. 19, no. 12, pp. 1438–1446, 2017.

29

[3]   L. Pinzur *et al.*, "Rescue from lethal acute radiation syndrome (ARS) with severe weight loss by secretome of intramuscularly injected human placental stromal cells," *J. Cachexia. Sarcopenia Muscle*, vol. 9, no. 6, pp. 1079–1092, 2018.

[4]   T. Winkler *et al.*, "Immunomodulatory placental-expanded, mesenchymal stromal cells improve muscle function following hip arthroplasty," *J. Cachexia. Sarcopenia Muscle*, vol. 9, no. 5, pp. 880–897, 2018.

[5]   T. H. Qazi, G. N. Duda, M. J. Ort, C. Perka, S. Geissler, and T. Winkler, "Cell therapy to improve regeneration of skeletal muscle injuries," *J. Cachexia. Sarcopenia Muscle*, vol. 49, 2019.

[6]   J. A. Ankrum, J. F. Ong, and J. M. Karp, "Mesenchymal stem cells: Immune evasive, not immune privileged," *Nat. Biotechnol.*, vol. 32, no. 3, pp. 252–260, 2014.

[7]   M. Riazifar, E. J. Pone, J. Lötvall, and W. Zhao, "Stem Cell Extracellular Vesicles: Extended Messages of Regeneration," *Annu. Rev. Pharmacol. Toxicol.*, vol. 57, no. 1, pp. 125–154, 2016.

[8]   M. Yáñez-Mó *et al.*, "Biological properties of extracellular vesicles and their physiological functions.," *J. Extracell. vesicles*, vol. 4, no. May, p. 27066, 2015.

[9]   C. Théry *et al.*, "Minimal information for studies of extracellular vesicles 2018 (MISEV2018): a position statement of the International Society for Extracellular Vesicles and update of the MISEV2014 guidelines," *J. Extracell. Vesicles*, vol. 7, no. 1, 2018.

[10]   G. van Niel, G. D'Angelo, and G. Raposo, "Shedding light on the cell biology of extracellular vesicles," *Nat. Rev. Mol. Cell Biol.*, vol. 19, no. 4, pp. 213–228, Apr. 2018.

[11]   T. Neri *et al.*, "CD18-mediated adhesion is required for the induction of a proinflammatory phenotype in lung epithelial cells by mononuclear cell-derived extracellular vesicles," *Exp. Cell Res.*, vol. 365, no. 1, pp. 78–84, Apr. 2018.

[12]   T. Lener *et al.*, "Applying extracellular vesicles based therapeutics in clinical trials - An ISEV position paper," *J. Extracell. Vesicles*, vol. 4, no. 1, 2015.

[13]   K. Schallmoser and D. Strunk, "Preparation of pooled human platelet lysate (pHPL)

30

as an efficient supplement for animal serum-free human stem cell cultures.," *Journal of visualized experiments JoVE*, no. 32. pp. 20–23, 2009.

[14] M. Colombo, G. Raposo, and C. Théry, "Biogenesis, Secretion, and Intercellular Interactions of Exosomes and Other Extracellular Vesicles," *Annu. Rev. Cell Dev. Biol.*, vol. 30, no. 1, pp. 255–289, Oct. 2014.

[15] S. Laner-Plamberger *et al.*, "Mechanical fibrinogen-depletion supports heparin-free mesenchymal stem cell propagation in human platelet lysate," *J. Transl. Med.*, vol. 13, no. 1, pp. 1–10, 2015.

[16] G. V. Shelke, C. Lässer, Y. S. Gho, and J. Lötvall, "Importance of exosome depletion protocols to eliminate functional and RNA-containing extracellular vesicles from fetal bovine serum," *J. Extracell. Vesicles*, vol. 3, no. 1, pp. 1–8, 2014.

[17] D. C. Watson *et al.*, "Scalable, cGMP-compatible purification of extracellular vesicles carrying bioactive human heterodimeric IL-15/lactadherin complexes," *J. Extracell. Vesicles*, vol. 7, no. 1, 2018.

[18] K. Pachler *et al.*, "An in vitro potency assay for monitoring the immunomodulatory potential of stromal cell-derived extracellular vesicles," *Int. J. Mol. Sci.*, vol. 18, no. 7, 2017.

[19] K. Schallmoser *et al.*, "Human platelet lysate can replace fetal bovine serum for clinical-scale expansion of functional mesenchymal stromal cells," *Transfusion*, vol. 47, no. 8, pp. 1436–1446, 2007.

[20] A. Reinisch *et al.*, "Epigenetic and in vivo comparison of diverse MSC sources reveals an endochondral signature for human hematopoietic niche formation," *Blood*, vol. 125, no. 2, pp. 249–260, 2015.

[21] A. Reinisch *et al.*, "A humanized bone marrow ossicle xenotransplantation model enables improved engraftment of healthy and leukemic human hematopoietic cells," *Nat. Med.*, vol. 22, no. 7, 2016.

[22] K. Schallmoser *et al.*, "Rapid large-scale expansion of functional mesenchymal stem cells from unmanipulated bone marrow without animal serum," *Tissue Eng. - Part C Methods*, vol. 14, no. 3, pp. 185–196, 2008.

31

October 17, 2019

[23] O. P. B. Wiklander *et al.*, "Systematic Methodological Evaluation of a Multiplex Bead-Based Flow Cytometry Assay for Detection of Extracellular Vesicle Surface Signatures.," *Front. Immunol.*, vol. 9, no. June, p. 1326, 2018.

[24] A. Görgens *et al.*, "Optimisation of imaging flow cytometry for the analysis of single extracellular vesicles by using fluorescence-tagged vesicles as biological reference material.," *J. Extracell. vesicles*, vol. 8, no. 1, p. 1587567, 2019.

[25] R. Crescitelli *et al.*, "Distinct RNA profiles in subpopulations of extracellular vesicles: apoptotic bodies, microvesicles and exosomes.," *J. Extracell. vesicles*, vol. 2, 2013.

[26] A. Reinisch *et al.*, "Humanized large-scale expanded endothelial colony-forming cells function in vitro and in vivo," *Blood*, vol. 113, no. 26, pp. 6716–6725, 2009.

[27] N. A. Hofmann, A. Reinisch, and D. Strunk, "Isolation and large scale expansion of adult human endothelial colony forming progenitor cells.," *Journal of visualized experiments JoVE*, no. 32. pp. 1–2, 2009.

[28] M. Taub, "The use of defined media in cell and tissue culture," *Toxicol. Vitr.*, vol. 4, no. 3, pp. 213–225, Jan. 1990.

[29] M. M. Lalu *et al.*, "Evaluating mesenchymal stem cell therapy for sepsis with preclinical meta-analyses prior to initiating a first-in-human trial," *Elife*, vol. 5, Nov. 2016.

[30] K. Schlosser *et al.*, "Effects of Mesenchymal Stem Cell Treatment on Systemic Cytokine Levels in a Phase 1 Dose Escalation Safety Trial of Septic Shock Patients," *Crit. Care Med.*, vol. 47, no. 7, p. 1, Feb. 2019.

[31] A. Flemming, K. Schallmoser, D. Strunk, M. Stolk, H.-D. Volk, and M. Seifert, "Immunomodulative efficacy of bone marrow-derived mesenchymal stem cells cultured in human platelet lysate.," *J. Clin. Immunol.*, vol. 31, no. 6, pp. 1143–56, 2011.

[32] N. Ketterl *et al.*, "A robust potency assay highlights significant donor variation of human mesenchymal stem/progenitor cell immune modulatory capacity and extended radio-resistance," *Stem Cell Res. Ther.*, vol. 6, no. 1, 2015.

[33] L. Kordelas *et al.*, "MSC-derived exosomes: a novel tool to treat therapy-refractory

32

graft-versus-host disease," *Leukemia*, vol. 28, no. 4, pp. 970–973, Apr. 2014.

[34] L. Kordelas *et al.*, "Individual Immune-Modulatory Capabilities of MSC-Derived Extracellular Vesicle (EV) Preparations and Recipient-Dependent Responsiveness," *Int. J. Mol. Sci.*, vol. 20, no. 7, p. 1642, Apr. 2019.

[35] J. Hartler *et al.*, "Deciphering lipid structures based on platform-independent decision rules," *Nat. Methods*, vol. 14, no. 12, pp. 1171–1174, Dec. 2017.

[36] S. Saito, K. Hiemori, K. Kiyoi, and H. Tateno, "Glycome analysis of extracellular vesicles derived from human induced pluripotent stem cells using lectin microarray," *Sci. Rep.*, vol. 8, no. 1, p. 3997, Dec. 2018.

[37] L. Tao *et al.*, "Metabolomics identifies serum and exosomes metabolite markers of pancreatic cancer," *Metabolomics*, vol. 15, no. 6, p. 86, Jun. 2019.

[38] G. Moll *et al.*, *Cryopreserved or fresh mesenchymal stromal cells: Only a matter of taste or key to unleash the full clinical potential of MSC therapy?*, vol. 951. 2016.

[39] M. Oeller *et al.*, "Selection of tissue factor-deficient cell transplants as a novel strategy for improving hemocompatibility of human bone marrow stromal cells," *Theranostics*, vol. 8, no. 5, 2018.

[40] E. Rohde, K. Pachler, and M. Gimona, "Manufacturing and characterization of extracellular vesicles from umbilical cord–derived mesenchymal stromal cells for clinical testing," *Cytotherapy*, vol. 21, no. 6, pp. 581–592, Jun. 2019.

[41] T. Burnouf, D. Strunk, M. B. C. Koh, and K. Schallmoser, "Human platelet lysate: Replacing fetal bovine serum as a gold standard for human cell propagation?," *Biomaterials*, vol. 76, 2016.

[42] A. Reinisch and D. Strunk, "Isolation and animal serum free expansion of human umbilical cord derived mesenchymal stromal cells (MSCs) and endothelial colony forming progenitor cells (ECFCs).," *Journal of visualized experiments JoVE*, no. 32. pp. 4–7, 2009.

[43] C. Bartmann *et al.*, "Two steps to functional mesenchymal stromal cells for clinical application.," *Transfusion*, vol. 47, no. 8, pp. 1426–35, 2007.

33

October 17, 2019

[44]   S. C. Taylor, T. Berkelman, G. Yadav, and M. Hammond, "A defined methodology for reliable quantification of western blot data," *Mol. Biotechnol.*, vol. 55, no. 3, pp. 217–226, 2013.

[45]   N. Koliha *et al.*, "A novel multiplex bead-based platform highlights the diversity of extracellular vesicles," *J. Extracell. Vesicles*, vol. 5, no. 1, p. 29975, Jan. 2016.

[46]   C. Tripisciano *et al.*, "Different Potential of Extracellular Vesicles to Support Thrombin Generation: Contributions of Phosphatidylserine, Tissue Factor, and Cellular Origin," *Sci. Rep.*, vol. 7, no. 1, p. 6522, Dec. 2017.

[47]   B. Fendl *et al.*, "Differential Interaction of Platelet-Derived Extracellular Vesicles With Circulating Immune Cells: Roles of TAM Receptors, CD11b, and Phosphatidylserine," *Front. Immunol.*, vol. 9, p. 2797, Dec. 2018.

[48]   R. Weiss *et al.*, "Differential Interaction of Platelet-Derived Extracellular Vesicles with Leukocyte Subsets in Human Whole Blood," *Sci. Rep.*, vol. 8, no. 1, p. 6598, Dec. 2018.

[49]   D. N. Mastronarde, "Automated electron microscope tomography using robust prediction of specimen movements," *J. Struct. Biol.*, vol. 152, no. 1, pp. 36–51, Oct. 2005.

[50]   J. Cox and M. Mann, "MaxQuant enables high peptide identification rates, individualized p.p.b.-range mass accuracies and proteome-wide protein quantification," *Nat. Biotechnol.*, vol. 26, no. 12, pp. 1367–1372, Dec. 2008.

[51]   The UniProt Consortium, "UniProt: the universal protein knowledgebase," *Nucleic Acids Res.*, vol. 45, no. D1, pp. D158–D169, Jan. 2017.

[52]   S. Tyanova *et al.*, "The Perseus computational platform for comprehensive analysis of (prote)omics data," *Nat. Methods*, vol. 13, no. 9, pp. 731–740, Sep. 2016.

[53]   M. E. Ritchie *et al.*, "limma powers differential expression analyses for RNA-sequencing and microarray studies.," *Nucleic Acids Res.*, vol. 43, no. 7, p. e47, 2015.

[54]   G. Yu, L.-G. Wang, Y. Han, and Q.-Y. He, "clusterProfiler: an R package for comparing biological themes among gene clusters.," *OMICS*, vol. 16, no. 5, pp. 284–7, 2012.

October 17, 2019

[55] N. A. Hofmann *et al.*, "Oxygen Sensing Mesenchymal Progenitors Promote Neo-Vasculogenesis in a Humanized Mouse Model In Vivo," *PLoS One*, vol. 7, no. 9, 2012.

Acknowledgements:

October 17, 2019

Table S1: Proteomic analysis sample preparation – pre-analytics.

Sample	Protein [mg/mL]	EV count [particles/mL]	Protein IDs [count] unlabelled
α-MEM*/TFF	1.5	1.18×10^8	631
P15 sol.F.	1.1	n.a.	405
P15 crude EVs	15.3	6.45×10^{10}	549
P15 pur. EVs	2.6	8.68×10^{10}	1,095
P25 sol.F.	1.5	n.a.	559
P25crude EVs	11.7	7.45×10^{10}	401
P25 pur. EVs	2.4	2.46×10^{11}	1,168
P27 sol.F.	1.3	n.a.	448
P27crude EVs	38.5	8.17×10^{10}	814
P27 pur. EVs	2.1	1.58×10^{11}	622

Table S3: Antibodies and dilutions used in western blots.

Name	Supplier	Clone	Isotype	Concentration	WB dilution
Apolipoprotein A1	GeneTex	polyclonal	IgG	0.66 mg/mL	1:1320
Calnexin	Cell Signaling	C5C9	IgG	26 µg/mL	1:1000
CD9	Invitrogen	MM2/57IVA50	IgG2	1 mg/mL	1:50
CD63	Thermo Fisher	TS63	IgG1	0.5 mg/mL	1:1000
CD81	Bio-Rad	1D6	IgG1	1 mg/mL	1:500
Flotillin 1	BD	Flotillin-1	IgG1	0.25 mg/mL	1:1000
GRP94	Bio-Rad	polyclonal	IgG	0.5 mg/mL	1:2000
Human Albumin	Thermo Fisher	KT11	IgG1	1 mg/mL	1:1000

October 17, 2019

Table S2: Quantitative Proteomic characterization of PLX secretome fractions.

Go terms used for labelling in Volcano Plot

Movement	Immune modulation	Angiogenesis	Extracellular vesicles
cell migration GO:0016477	regulation of inflammatory response GO:0050727	positive regulation of angiogenesis GO:0045766	endocytic vesicle lumen GO:0071682
morphogenesis of a polarized epithelium GO:0001738	regulation of immune effector process GO:0002697	sprouting angiogenesis GO:0002040	vesicle GO:0031982
actin filament organization GO:0007015	neutrophil mediated immunity GO:0002446	regulation of angiogenesis GO:0045766	transport vesicle GO:0030133
postsynaptic actin cytoskeleton organization GO:0098974	leukocyte migration GO:0050900	cell-substrate adhesion GO:0031589	vesicle-mediated transport GO:0016192
skeletal muscle contraction GO:0003009	humoral immune response GO:0006959	extracellular matrix organization GO:0030198	vesicle docking involved in exocytosis GO:0006904
microtubule-based process GO:0007017	antigen processing and presentation GO:0019882	positive regulation of angiogenesis GO:0045766	vesicle transport along microtubule GO:0047496
cell chemotaxis GO:0060326	complement activation GO:0006956	negative regulation of angiogenesis GO:0016525	vesicle fusion GO:0006906
	positive regulation of B cell activation GO:0050871	negative regulation of cell migration involved in sprouting angiogenesis GO:0090051	vesicle docking GO:0048278
		negative regulation of sprouting angiogenesis GO:1903671	vesicle docking involved in exocytosis GO:0006904
			exocytic vesicle GO:0070382
			transport vesicle membrane GO:0030658
			clathrin-coated vesicle membrane GO:0030665
			extracellular vesicle GO:1903561

October 17, 2019

highly enriched **sol. F.**   **pur. EV** highly enriched

Log10 adj. P value

log2 FC > 2   log2 FC > 2

Log2 Fold change pur. EV vs. sol.F

● Adj. P val. < 0.05 & log2 FC< -2   ● Not Significant   ● Adj. P val. < 0.05 & log2 FC > 2
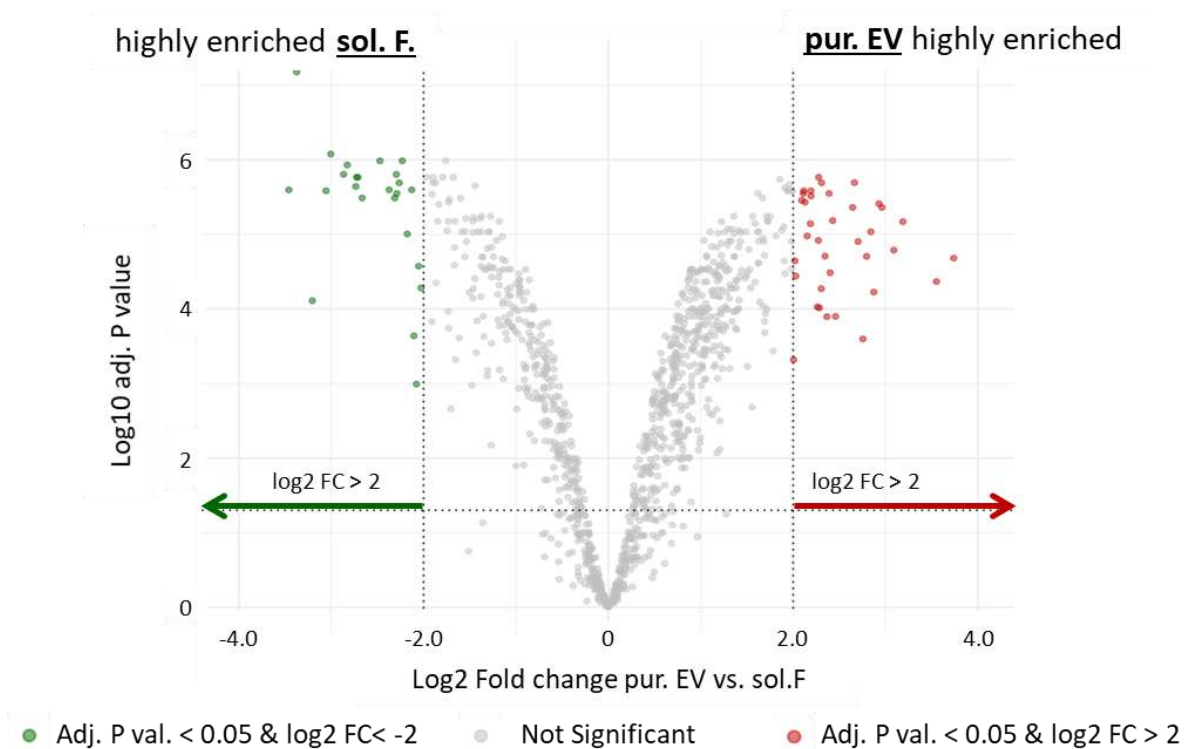
Gene	Protein name	log FC	Gene ontology	Uniprot ID	Gene	Protein name	log FC	Gene ontology	Uniprot ID
TTR	Transthyretin	-2.03	thyroid hormone transport [GO:0070327]	E9KL36	IgH	Ig heavy chain variable region	3.74		A0A2U8J8X8
	Myosin-reactive immunoglobulin light chain variable region	-2.05		Q9UL83	APOC1	Apolipoprotein C-I	3.55	lipoprotein metabolic process [GO:0042157]	K7ERI9
	Insulysin variant	-2.08	metal ion binding [GO:0046872]	Q59GA5		Apolipoprotein B variant	3.19		Q59HB3
	MS-C4 heavy chain variable region	-2.10		A0A125U0U9	HBA2	Mutant hemoglobin subunit alpha 2	3.09	oxygen carrier activity [GO:0005344]	A0A385HW63
	cDNA FLJ55606, highly similar to Alpha-2-HS-glycoprotein	-2.13	cysteine-type endopeptidase inhibitor activity [GO:0004869]	B7Z8Q2	ARF1	ADP-ribosylation factor 1, isoform CRA_a	2.96	very-low-density lipoprotein particle assembly [GO:0034379]	A0A024R3Q3
IGHV 3-20	Immunoglobulin heavy variable 3-20	-2.18	positive regulation of B cell activation [GO:0050871]	A0A0C4DH32		cDNA FLJ58310, highly similar to Homo sapiens trinucleotide repeat containing 15	2.93		B4DZM1
CALU	CALU protein	-2.23	calcium ion binding [GO:0005509]	Q6IAW5	RIC8A	Synembryn-A	2.87		E9PSI0
	Epididymis secretory sperm binding protein	-2.26	extracellular space [GO:0005615]	A0A384MDQ7	CLIP2	CAP-GLY domain containing linker protein 2	2.84		A7E2F7
SERPINA1	Alpha-1-antitrypsin	-2.29	extracellular space [GO:0005615]	A0A024R6I7	APOC3	Apolipoprotein C-III	2.79	lipoprotein metabolic process [GO:0042157]	A3KPE2
HEL-76	Epididymis luminal protein 76	-2.29	secretion [GO:0046903]	V9HW21	FASN	Fatty acid synthase	2.76	biosynthetic process [GO:0009058]	A0A0U1RQF0

October 17, 2019

Figure S5: Proteins most abundantly over-represented in purified EVs compared to the soluble factor fraction. Corresponding to proteins marked by open circles in Fig. 6. Proteins most abundant in purified (pur.) EVs marked in red; most abundant over-represented in the soluble factor (sol. F.) fraction marked in green. Top 10 hits selected in the adjacent table including details as identified.
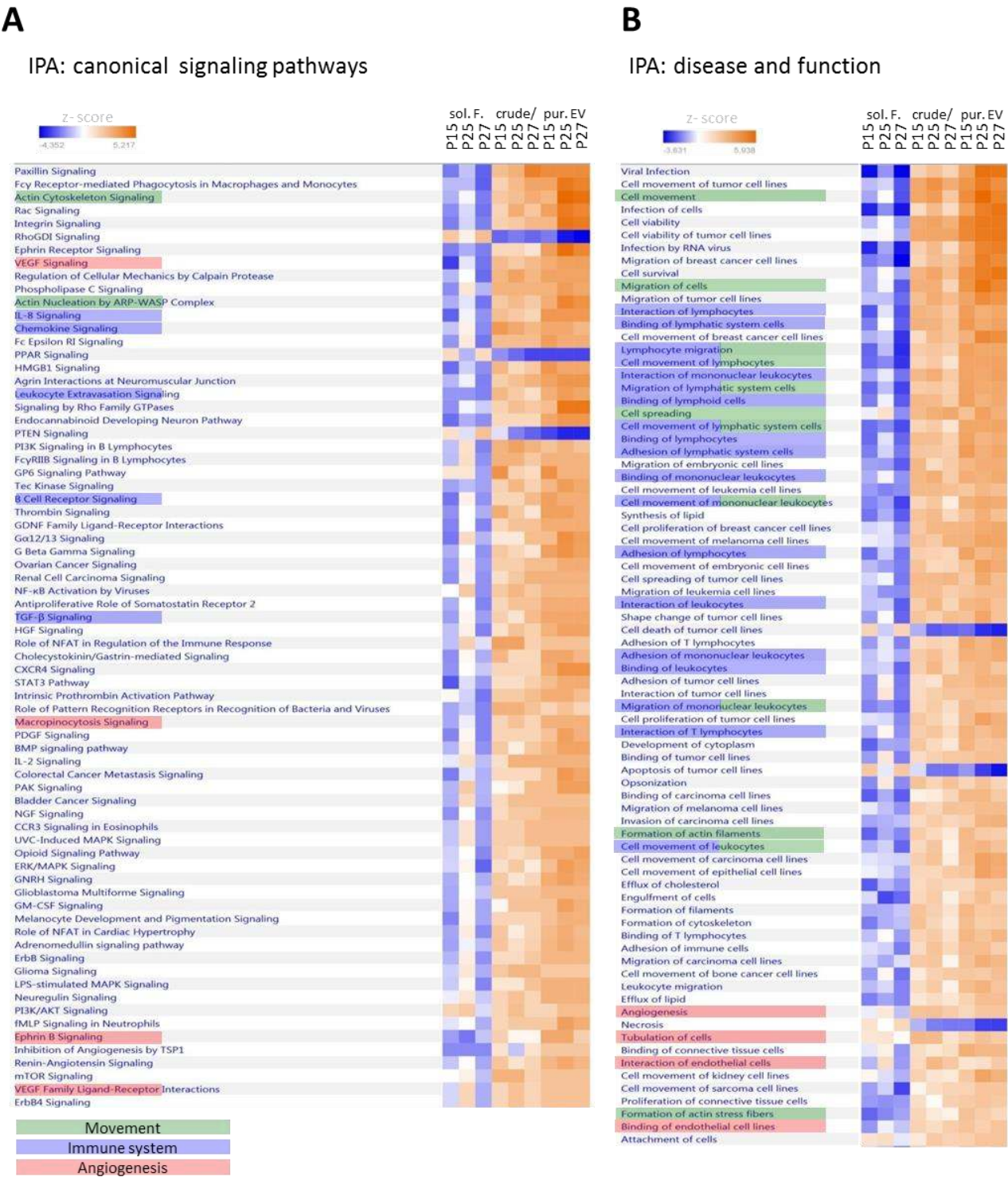

Figure S6: Ingenuity pathway (IPA) enrichment analysis of quantitative proteomics

October 17, 2019

of the PLX secretome fractions. (**A**) Canonical signaling pathways differentially abundant in EVs versus soluble factors (sol.F.) are shown in a heatmap for three individual donors (P15, P25, P27) analyzed. Pathways related to movement, the immune system and angiogenesis are colored green, blue and red, respectively, as indicated. (**B**) Disease and function categories from the ingenuity database with the greatest differences in corresponding protein abundances between EVs and soluble factor fractions are shown in a heatmap using the same color code for highlighting pathways.
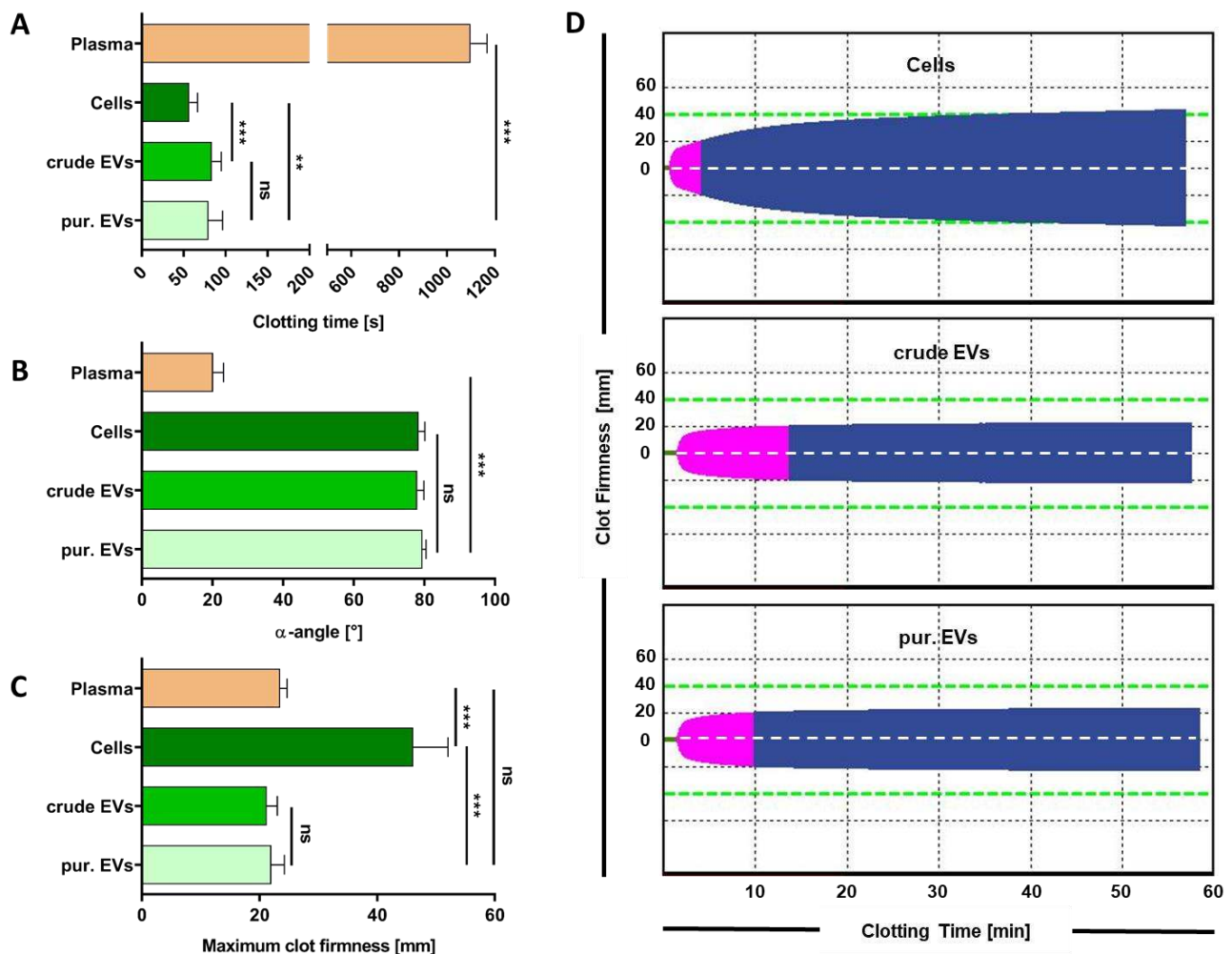

Figure S7: Comparison of coagulation activity of PLX cells vs. PLX-derived EVs. (**A**) Clotting time, (**B**) a-angle and (**C**) maximum clot firmness of reference plasma in the absence of cells or vesicles is shown compared to clotting behavior in the presence of one million PLX cells or one billion crude vs. purified (pur.) corresponding EVs as indicated. Results represent means of triplicate measurements from three independent donors ± SD. (**D**) Representative thromboelastometry curves plotting clot firmness over clotting time are shown.

October 17, 2019